Eidgenössische Technische Hochschule Zürich
Swiss Federal Institute of Technology Zurich

Diplomarbeit

Local Qubit Control in Circuit Quantum Electrodynamics

Presented by: Lars Steffen
Supervisor: Prof. Dr. Andreas Wallraff,
Laboratorium für Festkörperphysik, ETH Zürich

Zürich, May 28, 2008

Abstract

Circuit quantum electrodynamics (QED) [1] is the solid state version of cavity quantum electrodynamics, where the interaction of photons and atoms inside a cavity is studied. But instead of optical cavities and real atoms, a circuit QED system uses a one-dimensional transmission line resonator as a cavity [2] and a Cooper pair box [3] as an artificial atom. These systems are not only intresting because they offer the possibility to perform quantum optic experiments in a solid state system, but also because they are a promising candidate for the implementation of a quantum information processor. In recent realizations of such circuit QED experiments [4, 5], single qubits could be well characterized and controlled. Even the coupling of two qubits via the cavity has been achieved [6].

In a next step towards the implementation of a quantum information processor, one needs to perform experiments with many qubits. For that case, one has to be able to control the parameters of each qubit individually. This means that one should be able to change the state of a qubit without disturbing the other ones and also to tune the transition frequency of each qubit separately. So far, the qubits were driven by microwave signals applied to the resonator. In that case, the control parameters couple to all qubits resulting in a bad selectivity. The qubit transition frequency can be adjusted by a magnetic flux through the loop of the Cooper pair box. This was accomplished by an external coil. To be able to control several qubits independently of each other, one has to use on-chip gatelines for each qubit instead of coupling a bias voltage and RF signal via the resonator or applying a global magnetic field.

One of the main goals of this thesis was to design new gate lines for local qubit control and calculate their effects on the decay time. To control the qubit state, lines similar to the ones that couple to the resonator can be used. These lines couple directly and therefore stronger to the Cooper pair boxes. The stroger coupling allows to drive transitions faster than via the resonator but offers also a direct decay channel for the qubit state. The final design of the charge/drive lines was a tradeoff between high control ability and long decay times.

The control of the qubit transition frequncy by magnetic flux is more challenging. To generate a flux, one needs a current passing near by the Cooper pair box. But the low mutual inductance of such a line requires high currents to achieve a reasonnable control ability. To prevent the low temperature stages of the cryostat from heating up, a new cabling with low resistance components had to be implemented.

This thesis presents the designs of gate lines for local qubit control. To estimate the

effects of these gates to the decay rate of a Cooper pair box, a formalism was developped which allows to calculate the relaxation time and the coupling strength. For the cabling of the crystat, a concept for the additional wiring has been worked out. First chips with the new gate lines have been fabricated and the microwave characterization and the cross couplings are discussed.

Contents

1 Introduction

Quantum information processing is a relatively new field in physics. It was only since the last two decades of the 20^{th} century, where physicist realized that quantum mechanics could be used to create a new way of computation. It was Feynman [7] in 1982, who brought up the idea of a quantum computer as a device which takes advantage of the effects of quantum mechanics such that it might perform more powerful calculations than a classical computer (Turing machine). One important application which Feynman pointed out already could be the ability of simulating quantum systems. The first description of a universal quantum computer and investigations of its properties were done in 1985 by Deutsch [8]. For some time, the research in this field was mainly of theoretical nature. In 1992, Deutsch and Josza [9] presented an algorithm that is faster on a quantum computer than on a classical computer, and in 1994, Shor [10] demonstrated an algorithm that is able to factorize large numbers in polynomial time on a quantum computer. This is in particular interesting, because the safety of most modern algortithms for cryptography relies on the unability of classical computers to perform this task in an efficient way. Another example is Grover's search algorithm [11], which can search entries in large databases faster than any classical algorithm.

In the following, a search for an experimental realization of such a quantum computer and its basic units of information, the quantum bits (qubits) [12], has begun. Like classical bits, qubits can take the value "0" or "1", but in addition, any superposition state is allowed too. The implementation of such a qubit requires quantum mechanical two-level systems that can be well controlled and measured. Possible implementations of such qubits are e. g. the electronic states of trapped ions [13], electron spins in quantum dots [14], nuclear spins used in NMR quantum computation [15] and a superconducting circuit, known as Cooper pair box [3].

Due to the third law of thermodynamics, a finite system always has a non-zero entropy. A physical state will therefore always have some interaction with its environment. These external disturbances destroy the unitary evolution and reversibility, which change a pure state into a mixed state. This process is called decoherence and is one of the main obstacles in implementing a quantum computer. A good isolation of the qubit form its environment is therefore necessary such that it has a long coherence time, which allows to perform many operations before the information is lost. Nevertheless, a totally isolated system cannot be used as a quantum computer either, because one has to be able to prepare an initial state of the qubits, to perform operations and to measure the result.

One promising approach towards quantum computing which allows to isolate the qubits efficiently from the environment while still providing good measurement and control possibilities is called *Circuit quantum electrodynamics* [1, 4]. This is a solid state version of optical cavity quantum electrodynamics (QED), where the interaction of atoms with photons inside a cavity is studied. In circuit QED, a Cooper pair box is coupled to a microwave cavity, which is realized with a one-dimensinal transmission line resonator [16]. By applying microwave signals to the resonator, one can couple the photons in the cavity with the qubit, which allows to coherently control or measure the qubit state.

The aim of this diploma thesis is to design and implement local gatelines which will allow to control the qubit state directly (not via the resonator) and to control the qubit transition frequency. These gates will also offer new decay channels for the qubit state which reduce the coherence time. Therefore it is important to be able to estimate the effects of the new gate lines to the coherence time.

Chapter 2 presents a review of the theory behind the Cooper pair boxes, coplanar waveguide resonators and cavity QED systems. Chapter 3 explains how the control of the qubit works and introduces ideas how to implement local control gate lines. In chapter 4, the local drive/charge line is discussed in detail. To understand the effects of these lines to the decoherence times, a formalism to calculate the expected decay time is worked out. Based on these calculations, the design of the gateline was chosen. The local flux line to control the qubit transition frequencies are discussed in chapter 5. Due to the higher current that is needed to generate a flux, new wiring in the cryostat is needed for these lines in order to prevent a heating up of the lowest temperature stages. This is presented in chapter 6. Finally chapter 7 discusses measurements of the microwave characterization of some of the resonators with the new gate lines and the cross coupling of the resonators with the gates.

2 Theory

2.1 Quantum bits

A quantum bit ("qubit") is a unit of quantum information [12]. It is a quantum system in which the Boolean states "0" and "1" are represented by a pair of normalized and orthogonal quantum states labeled as $\{|0\rangle, |1\rangle\}$ (denoted as "ground state" and "excited state"). Unlike a classical bit which can be either "0" or "1", a qubit can be in any superposition state $\alpha|0\rangle + \beta|1\rangle$ for some α and β such that $|\alpha|^2 + |\beta|^2 = 1$.

A common visualization of a qubit state is the so called Bloch sphere representation. A (pure) qubit state $|\psi\rangle$ can be written as

$$|\psi\rangle = \cos\frac{\theta}{2}|0\rangle + e^{i\varphi}\sin\frac{\theta}{2}|1\rangle$$

with $0 \leq \theta \leq \pi$ and $0 \leq \varphi \leq 2\pi$. The two variables θ and φ define a point on the surface of a three-dimensional unit sphere. This is the Bloch sphere.

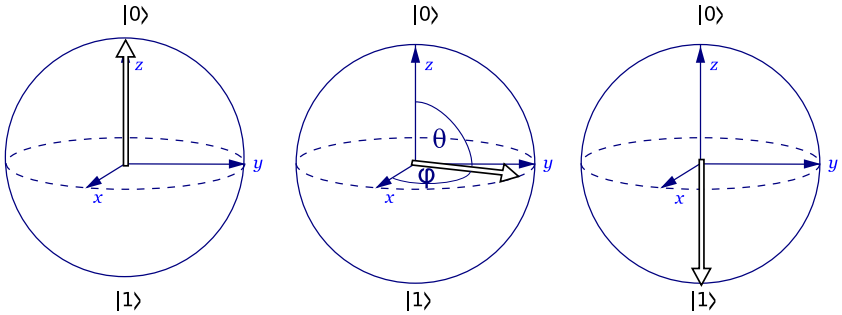

Figure 2.1: Bloch sphere representation of three different qubit states: Ground state, equal superposition state with phase φ and excited state.

2.2 Realization of the qubit

There are various ways of implementing a qubit. The implementation which is used in this work is a superconducting qubit embedded into a microwave resonator [4, 5, 1]. The following subsections will explain how a qubit is realised with a Cooper pair box and what improvements concerning tunability and noise sensitivity have been achieved so far.

2.2.1 Cooper pair box

A Cooper pair box (CPB) [3] consists of a superconducting electrode, called "island", connected to a superconducting reservoir by a Josephson tunnel junction with capacitance C_J and Josephson energy E_J. The Josephson junction can be thought of as a circuit element which allows Cooper pairs to coherently couple between the island and reservoir, with a stray capacitance in parallel. A gate voltage (V_g) can be used to electrostatically induce Cooper pairs to tunnel (cf. Fig. 2.2).

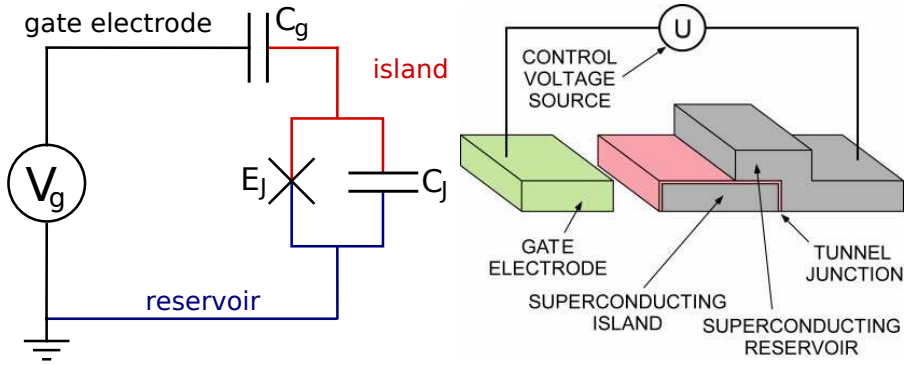

Figure 2.2: The Cooper pair box. Left: Circuit diagram. Right: Sketch of the simplest version of this circuit in which the superconducting island is coupled to a superconducting reservoir through a Josephson tunnel junction and to a gate electrode by a capacitor [2].

The only degree of freedom in this system is the number of excess Cooper pairs on the island n. The eigenstates $|n\rangle$ of the associated operator $\hat{n}$ form a complete basis for the state of the CPB. The Hamiltonian of the system can be written as a sum of an electrostatic part $H_{\rm el}$ and a part H_J which describes the coherent tunneling of Cooper pairs across the junction. In terms of the number basis, the Hamiltonian can be written as

$$\begin{aligned} \hat{H}_{\rm CPB} &= 4E_C(\hat{n}-n_g)^2 - E_J\cos\hat{\varphi} \\ &= \underbrace{4E_C(\hat{n}-n_g)^2}_{H_{\rm el}} + \underbrace{\frac{E_J}{2}\sum_N\left(|n\rangle\langle n+1| + |n+1\rangle\langle n|\right)}_{H_J}, \end{aligned} \tag{2.1}$$

where $E_C = e^2/2C_\Sigma$ is the electrostatic charging energy, $C_\Sigma = C_J + C_g$ the total capacitance of the CPB, $n_g = C_gV_g/2e$ the dimensionless gate charge and E_J the Josephson coupling energy. In the charge basis, the Schrödinger equation of the CPB can only be solved numerically. An analytical solution in terms of Mathieu characteristic functions can be found by writing the Hamiltonian 2.1 in the phase basis (see Ref. [1]).

In the charge regime ($4E_C \gg E_J$) where the conventional Cooper pair boxes are operated, fluctuations in the gate charge n_g (e.g. due to noise on the gate voltage) lead to fluctuations in the qubit transition frequency. At the degeneracy point $n_g = 1/2$,

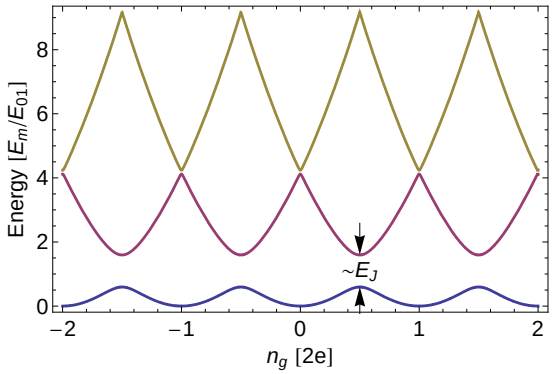

Figure 2.3: Energy level diagramm of a Cooper pair box. The (from bottom to top) blue, red, and yellow bands show the ground, and first two excited state energy levels with $E_J = E_C$. Energies are given in units of the transition energy E_{01}, evaluated at the degeneracy point $n_g = 1/2$ [17].

often referred to as the sweet spot, it is in first order immune against those fluctuations and allows to reach longer coherence times [18].

2.2.2 Split Cooper pair box

In the Hamiltonian (2.1), the electrostatic component can be tuned by applying a gate voltage (V_g), but the tunneling part of the Hamiltonian (H_J) remains unaffected. A tuning of the Josephson energy can be achieved by using a split Josephson junction, each part of which has its characteristic tunneling energy (E_{J1}, E_{J2}) and superconducting phase (θ_1, θ_2) across it (cf. Fig. 2.4). The Josephson part of the split CPB in terms of the phase basis is

$$\hat{H}_J = E_{J1} \cos \hat{\theta}_1 + E_{J2} \cos \hat{\theta}_2. \tag{2.2}$$

Introducing the following new variables

$$\theta = \frac{\theta_1 + \theta_2}{2},$$
$$\varphi = \theta_1 - \theta_2 = 2\pi\Phi/\Phi_0,$$

where $\Phi_0 = h/2e$ is the flux quantum, and using trigonometric substitutions, one can rewrite Eq. (2.2) as

$$\hat{H}_J = (E_{J1} + E_{J2}) \cos\left(\pi \frac{\Phi}{\Phi_0}\right) \cos\hat{\theta} + (E_{J2} - E_{J1}) \sin\left(\pi \frac{\Phi}{\Phi_0}\right) \sin\hat{\theta}. \tag{2.3}$$

If the junctions are symmetric ($E_{J1} = E_{J2}$) one can rewrite the expression to a single junction Hamiltonian with an effective phase tunable Josephson energy

$$E_J^{\text{eff}} = (E_{J1} + E_{J2}) \cos\left(\pi \frac{\Phi}{\Phi_0}\right). \tag{2.4}$$

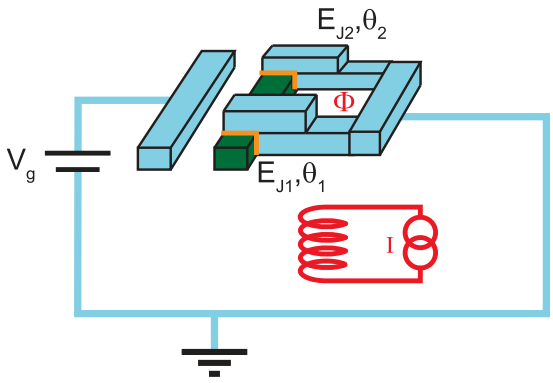

Figure 2.4: Sketch of the split Cooper pair box. The island (green) is connected to a reservoir by two junctions, each with a Josephson energy E_{J1}, E_{J2} and phase difference θ_1, θ_2. Splitting the box gives the ability to tune the effective $E_J = (E_{J1} + E_{J2})\cos(\pi\Phi/\Phi_0)$ by applying a magnetic flux Φ [17].

2.2.3 Transmon

As mentionned above, the conventional Cooper pair box is sensitive to fluctuations of the gate charge n_g. However, for increasing E_J/E_C ratio, the energy levels become exponentially flat [19], see Fig. 2.5, which makes the qubit transition frequency immune to charge fluctuations. A decrease of the charging energy can be achieved by enlarging the capacitance between the island and the reservoir. This leads to much larger linear dimensions of the CPB as shown in Fig. 2.6. These improved Cooper pair boxes are refered to as "transmons".

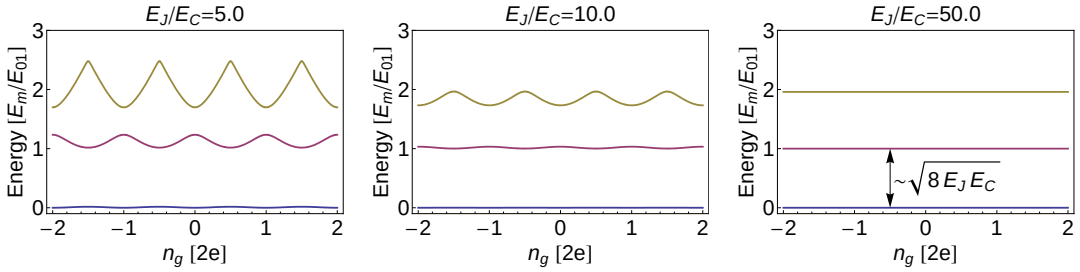

Figure 2.5: Energy level diagramm for the first three levels as a function of the effective offset charge n_g for different ratiosE_J/E_C. Energies are given in units of the transition energy E_{01}, evaluated at the degeneracy point $n_g = 1/2$ [19].

2.3 Microwave cavity

In circuit quantum electrodynamics (cf. section 2.4), the Cooper pair box is coupled to a cavity made of an electrical circuit. In the microwave regime, such a cavity can

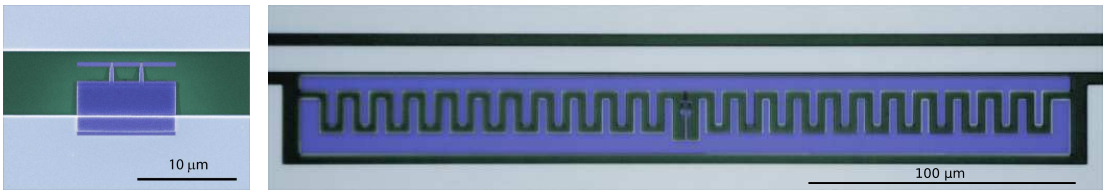

Figure 2.6: Comparison of the geometry of a conventional split CPB (left) and a transmon (right).

be realized with a one-dimensional transmission line resonator. This section therefore discusses the properties of such a transmission line resonator and a physical realization of it, called coplanar waveguide resonator.

2.3.1 Transmission line resonator

Schematically, a transmission line [16, chap. 2] can be represented as a two-wired line. To understand the properties, one can model this transmission line as consisting of many small lumped elements that have the same impedance per unit length as the transmission line (see Fig. 2.7). The impedance of one small section is

$$Z_0 = \sqrt{\frac{R_\ell + i\omega L_\ell}{G_\ell + i\omega C_\ell}},$$

where R_ℓ is the resistance per unit length due to conductor losses, L_ℓ is the inductance per unit length, G_ℓ is the shunt conductance per unit length due to dielectric losses between the conductor, and C_ℓ is the capacitance per unit length between the two wires.

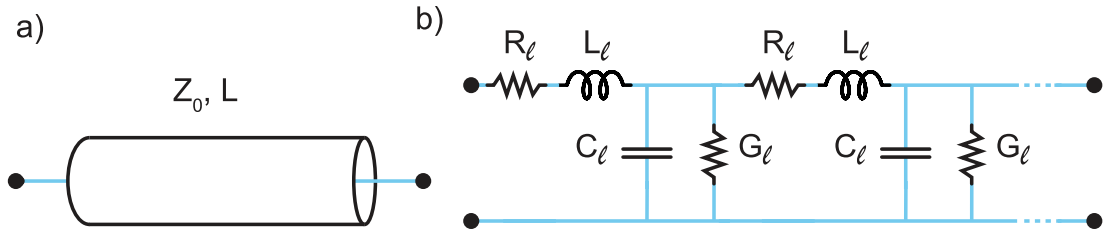

Figure 2.7: a) A transmission line with characteristic impedance Z_0 and length L. b) A transmission line can be modeled as an infinete series of lumped elements which have the correct resistances (R_ℓ), inductances (L_ℓ), conductances (G_ℓ), and capacitances (C_ℓ) per unit length.

In a lossless case, the impedance simplifies to $Z_0 = \sqrt{L_\ell/C_\ell}$. A signal propagates through a transmission line as a wave with complex propagation constant $\gamma = \alpha + i\beta = \sqrt{(R_\ell + i\omega L_\ell)(G_\ell + i\omega C_\ell)}$. The imaginary part β of the propagation constant describes the phase of the wave and the real part α describes the attenuation.

The effective input impedance of an arbitrary load Z_L at distance ℓ through a transmission line of characteristic impedance Z_0 is

$$Z_\mathrm{in} = Z_0 \frac{Z_\mathrm{L} + Z_0 \tanh \gamma\ell}{Z_0 + Z_\mathrm{L} \tanh \gamma\ell}.$$

When the load impedance is open or very large ($Z_0 \to \infty$) or a short ($Z_0 \to 0$), this expression simplifies to

$$Z_\mathrm{in}^\mathrm{open} = -Z_0 \coth \gamma\ell,$$
$$Z_\mathrm{in}^\mathrm{short} = Z_0 \tanh \gamma\ell.$$

A transmission line resonator is transmission line with open ends on both sides. In this case, two different types of resonance exist. Whenever the length of the line is an integer of a half wavelength ($\ell = n\lambda/2 = \pi v/\omega_0$), there will be a high impedance resonance. Whenever the length is an odd multiple of a quarter wavelength ($\ell = (2n+1)\lambda/4$), there will be a high admittance resonance. In the setup used in this diploma thesis, the $\lambda/2$ high impedance resonance has been used for which the resonace frequency is

$$\omega_{0,n}^\mathrm{open} = \frac{n\pi}{\ell\sqrt{L_\ell C_\ell}}.$$

Approximating the input impedance for around ω_0 and for small losses α gives

$$Z_\mathrm{in} = \frac{Z_0}{\alpha\ell + i\pi\frac{\omega-\omega_0}{\omega_0}}.$$

This formula has the same structure as the one of an RLC-oscillator with substitutions

$$R = \frac{Z_0}{\alpha\ell}, \tag{2.5}$$
$$C = \frac{\pi}{2\omega_0 Z_0}, \tag{2.6}$$
$$L = \frac{2Z_0}{\pi\omega_0}. \tag{2.7}$$

2.3.2 Capacitive coupling

In the previous subsection a transmission line resonator isolated from the environment is discussed. To be able to drive the resonator and to perform transmission measurements, one has to connect the resonator to the outside world. Just connecting another transmission lines directly at the in- and output would not be a good idea because this would allow the radiation to escape quickly by shunting the effective impedance to Z_0 and destroying the Q. A better approach is to connect the in- and output with transmission lines via small capacitors which causes a large impedance mismatch. This has an effect like a "mirror" for the photons, because it reflects most of the photons but transmits a small amount. This coupling affects the resonator by adding an effective capacitance C_κ

which shifts the resonance frequency, and an effective parallel resistance $1/G_{\text{ext}}$ which changes the Q. The effective shunt conductance G_{ext} on resonance is given by

$$G_{\text{ext}} = \Re(Y_{\text{in}}) = \Re\left(\frac{i\omega_n C_\kappa}{1 + i\omega_n C_k R_L}\right) = \frac{R_L C_\kappa^2 \omega_n^2}{1 + R_L^2 C_\kappa^2 \omega_n^2}, \tag{2.8}$$

where C_κ is the coupling capacitor and R_L the external load (see Fig. 2.8). The external

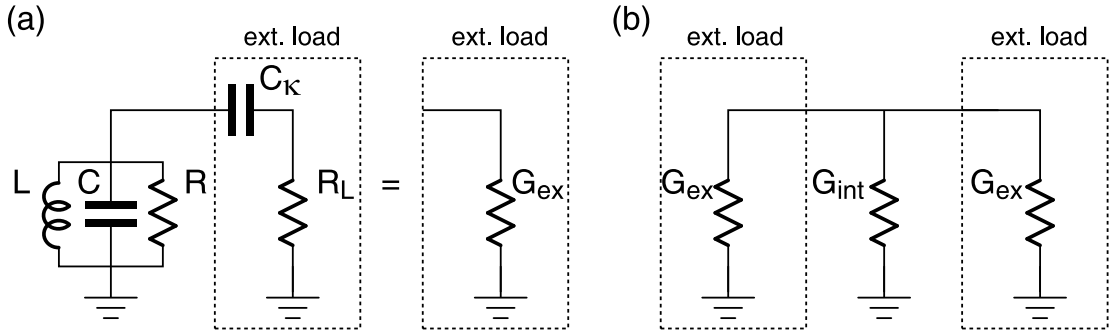

Figure 2.8: a) RLC-resonator coupled by a capacitor C_κ to a load R_L. b) Resonator coupled to input and output lines. [20]

quality factor can then be defined as

$$Q_{\text{ext}} = \frac{\omega_n C_n}{G_{\text{ext}}} \tag{2.9}$$

where C_n is the capacitance defined in Eq. (2.6). If the resonator is symmetrically coupled to the in- and output this expression becomes $Q_{\text{ext}} = \omega_n C_n / 2G_{\text{ext}}$, which can be rewritten as

$$Q_{\text{ext}} = \frac{n\pi}{4Z_0}\left(\frac{1}{C_\kappa^2 R_L \omega_n^2} + R_L\right). \tag{2.10}$$

The loaded quality factor Q_L of the resonator can be found considering the parallel connection of the internal quality factor Q_{int} and the external quality factor Q_{ext}

$$\frac{1}{Q_L} = \frac{1}{Q_{\text{int}}} + \frac{1}{Q_{\text{ext}}}, \tag{2.11}$$

where $Q_{\text{int}} = \omega_n C_n / G_{\text{int}}$.

2.3.3 Coplanar waveguide resonator

One possibel physical realization of such a transmission line is a coplanar waveguide (CPW) which is a 2D version of a coaxial line, having the ground in the same plane as the center pin as shown in Fig. 2.9. The characteristic impedance is determined by ratio a/b (see Fig. 2.9), the substrate height h, and the dielectric constant of the substrate ϵ_{r} [21]

$$Z_0^{\text{CPW}} = \frac{60\pi}{\sqrt{\epsilon_{\text{eff}}}} \frac{1}{\frac{K(k)}{K(k')} + \frac{K(k_3)}{K(k_3')}}, \tag{2.12}$$

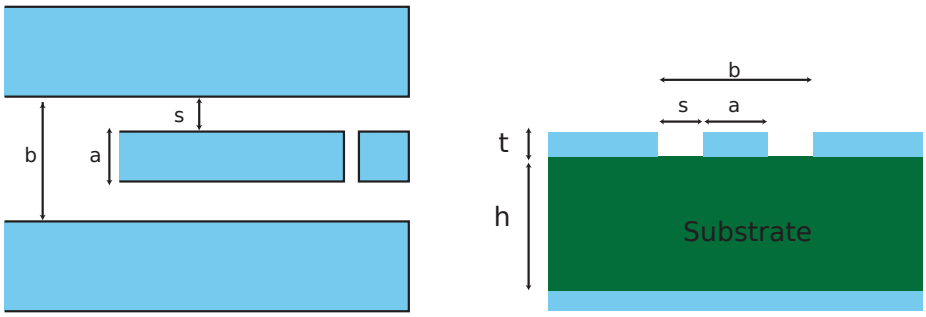

Figure 2.9: A conductor backed coplanar waveguide. The ratio a/b and the dielectric constant of the substrate ϵ_{r} determines the characteristic impedance Z_0. [17]

with the effective dielectric constant

$$\epsilon_{\mathrm{eff}} = \frac{1 + \epsilon_r \widetilde{K}}{1 + \widetilde{K}}, \tag{2.13}$$

where K is the complete elliptic integral of the first kind and

$$\widetilde{K} = \frac{K(k')K(k_3)}{K(k)K(k_3')}, \tag{2.14}$$

$$k = \frac{a}{b}, \tag{2.15}$$

$$k_3 = \frac{\tanh\left(\frac{\pi a}{4h}\right)}{\tanh\left(\frac{\pi b}{4h}\right)}, \tag{2.16}$$

$$k' = \sqrt{1 - k^2}, \tag{2.17}$$

$$k_3' = \sqrt{1 - k_3^2}. \tag{2.18}$$

2.4 Circuit quantum electrodynamics

This section describes how the Cooper pair box and the transmission line resonator can be coupled to a system that behaves similar to an atom in an optical cavity and that can be used to control and read out the state of the Cooper pair box.

2.4.1 Cavity quantum electrodynamics

Cavity quantum electrodynamics (CQED) studies the interaction of atoms with discrete photon modes in a cavity. A prototype system for this is a two-level atom which couples to the cavity, described by a harmonic oscillator whose excitations are photons. The dynamics of such a system can be described by the Jaynes-Cummings Hamiltonian [22, 1]

$$H_{\mathrm{JC}} = \hbar\omega_r(a^\dagger a + 1/2) + \hbar\frac{\omega_a}{2}\sigma_z + \hbar g(a^\dagger\sigma^- + a\sigma^+) + H_\kappa + H_\gamma. \tag{2.19}$$

The first term represents the energy of the electromagnetic field where each photon contains an energy $\hbar\omega_r$. The second term represents the atom as a spin-1/2 particle with transition energy $\hbar\omega_a$. The third term describes the dipole interaction where the atom can absorb ($a\sigma^+$) or emit ($a^\dagger\sigma^-$) a photon from/to the field at rate g. These three terms describe the coherent dynamics, whereas the last two terms describe decoherence effects due to the coupling of the cavity to the continuum which produces the cavity decay rate $\kappa = \omega_r/Q$, and due to the coupling of the atom to modes other than the cavity mode which cause the excited state to decay at rate γ (see Fig. 2.10).

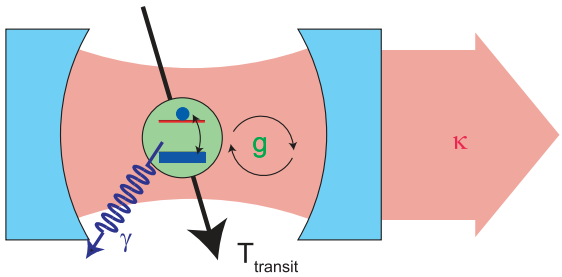

Figure 2.10: A two level atom coherently interacts with the cavity at a rate g. Also illustrated are decoherence processes that allow the photon to decay at a rate κ, the atom to decay at rate γ and the rate at which the atom leaves the cavity, $1/T_{\mathrm{transit}}$. To reach strong coupling limit, the interaction rate must be larger than the rates of decoherence $g > \kappa, \gamma, 1/T_{\mathrm{transit}}$ [17].

In the case of zero detuning ($\Delta = \omega_r - \omega_a = 0$) between the atom and the cavity, the eigenstates of the Jaynes-Cummings Hamiltonian (in the absence of damping) are the maximally entangled atom-field states $\left|\overline{\pm,0}\right\rangle = (|\uparrow,1\rangle \pm |\downarrow,0\rangle)/\sqrt{2}$. An initial state with an excited atom and zero photons $|\downarrow,0\rangle$ will therefore flop into a photon $|\uparrow,1\rangle$ and back again at the vacuum Rabi frequency g/π. Since the excitation is half atom and half photon, the decay rate of $\left|\overline{\pm,0}\right\rangle$ is $(\kappa+\gamma)/2$. When many oscillations can be completed before the atom decays or the photon is lost, the system reaches the strong coupling limit of cavity QED ($g > \kappa, \gamma, 1/T_{\mathrm{transit}}$) [1].

2.4.2 CQED with superconducting circuits

Cavity QED systems are not restricted to optical systems but can also be built out of circuits [1]. As a cavity one can use a one-dimensional transmission line resonator

as discussed in section 2.3 and as an artificial atom a Cooper pair box which couples capacitively to the electromagnetic field of the resonator. Fig. 2.11 shows a schematic representation of such a system. A Cooper pair box is placed between the transmission line and one of the ground planes near an antinode of the voltage standing wave. The island of the Cooper pair box lies near the center conductor of the resonator, which acts as a gate electrode for the Cooper pairs tunneling between the island and the reservoir. This allows to apply a DC voltage at the center conductor of the resonator via capacitive coupling over the input gap capacitance and therefore apply a gate voltage V_{DC} to the CPB via the capacitance between the center conductor and the island. In addition to this voltage, there is a quantum voltage due to photons inside the resonator.

$$V_{\mathrm{g}} = V_{\mathrm{DC}} + \hat{V}, \tag{2.20}$$

where $\hat{V} = \hat{q}/C$. This leads to

$$\hat{V} = \sqrt{\frac{\hbar\omega_{\mathrm{r}}}{2C}}(a + a^{\dagger}) = V_0(a + a^{\dagger}), \tag{2.21}$$

with V_0 the rms vacuum fluctuations. Plugging this into the elecrostatic part H_{el} of the CPB-Hamiltonian 2.1 one can find a coupling term which describes the cavity-CPB coupling and depends on the CPB state (via $\hat{N}$) and the quantum field state of the resonator (via $\hat{V}$):

$$H_{\mathrm{coup}} = 2\hbar g(a^{\dagger} + a)\hat{N}, \tag{2.22}$$

$$g = \frac{eV_0}{\hbar}\beta, \tag{2.23}$$

where β is the voltage division in the CPB. The coupling constant $2\hbar g$ can be seen as the energy of moving a Cooper pair across the portion of the rms vacuum voltage fluctuations (V_0) in the resonator. If one performs a rotating wave approximation, i. e. neglecting the rapidly rotating terms $a^{\dagger}\sigma^{+}$ and $a\sigma^{-}$, one obtains

$$H_{\mathrm{coup}} = \hbar g(a^{\dagger}\sigma^{-} + a\sigma^{+}). \tag{2.24}$$

This term appears together with the Hamiltonians for the CPB and the resonator in the Jaynes-Cummings Hamiltonian Eq. 2.19.

2.4.3 Readout scheme

A readout of the qubit state is possible in the dispersive regime, when the qubit transition frequency is strongly detuned from the resonator frequency, $\Delta = \omega_{\mathrm{a}} - \omega_{\mathrm{r}} >> g^2$. In this regime the qubit-resonator interaction in the Jaynes-Cummings Hamiltonian Eq. (2.19) can be treated perturbatively. The effective Hamiltonian up to second order is then [1]

$$H_{\mathrm{eff}} \simeq \hbar\left(\omega_{\mathrm{r}} + \frac{g^2}{\Delta}\sigma^z\right)a^{\dagger}a + \frac{\hbar}{2}\left(\omega_{\mathrm{a}} + \frac{g^2}{\Delta}\right)\sigma^z. \tag{2.25}$$

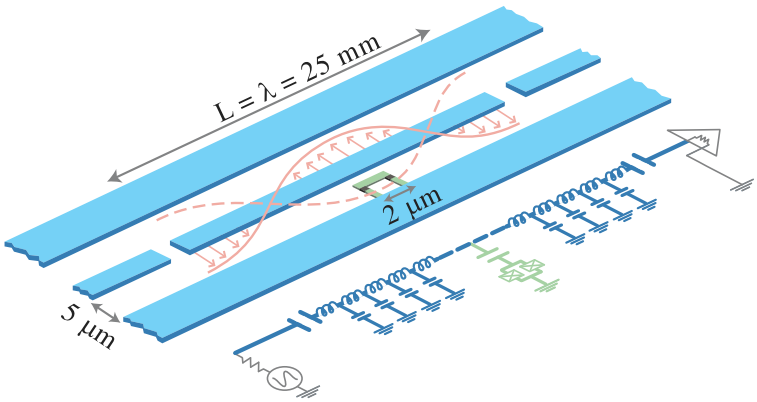

Figure 2.11: Schematic representation of the cooper pair box (green) and the coplanar waveguide resonator (blue) [1].

This expression shows, that the interaction between the qubit and the cavity leads to shift in the resonator frequency which gives an effective resonator frequency $\omega_r' \approx \omega_r \pm g^2/\Delta$ depending on the state of the qubit. This means that the qubit state is mapped onto the effective resonance frequency of the cavity. This shift of the cavity frequency can be probed by measuring the phase of a transmitted microwave (see Fig. 2.12). The phase shift is expected to be [1] $\delta\Phi = \arctan[2g^2/(\kappa\Delta)]$. A necessary condition to resolve the two states is that $\kappa \sim g^2/\Delta$ or smaller, which means that the linewidth of the output microwave has to be at least in the order of the frequency shift that arises when the qubit changes its state.

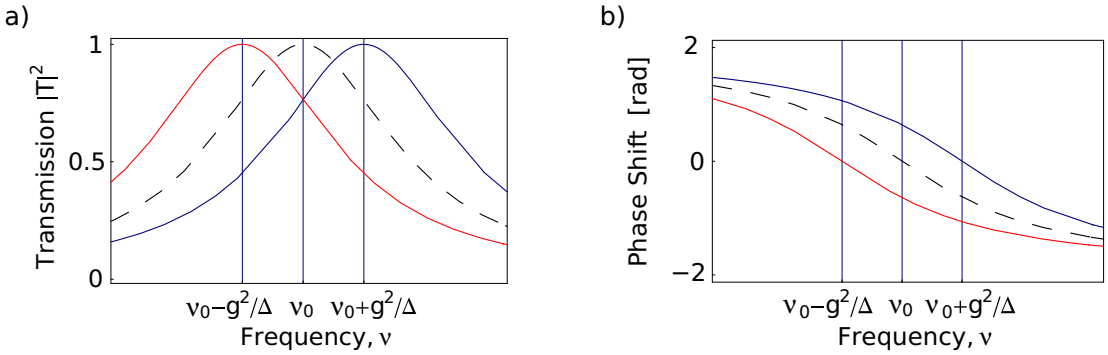

Figure 2.12: Amplitude a) and phase b) of the transmission spectrum of the cavity for ground (red) and excited (blue) qubit state. The black dashed line represents the cavity in absence of the CPB.[23].

2.5 Experimental setup

Figure 2.13 shows a schematic representation of the experimental setup. The transmission line resonator with the Cooper pair box is in a dilution refrigerator at a temperature of ~ 15 mK, whereas the microwaves for control and readout are generated at room temperature.

The shapes of the control microwave pulses are generated with an arbitrary waveform generator (AWG) which is capable of generating pulses with 1 ns resolution. The AWG is connected via an upconversion two quadrature (I,Q) mixer with the microwave generator. The RF signals are filtered and attenuated several times to minimize thermal noise. The DC signals are low-pass filtered with stainless steel powder filters (see section 6.2) at different temperature stages.

The qubit state is measured by determining the phase and the amplitude of a coherent microwave beam transmitted through the resonator at a frequency ω_{RF}, which is nearly resonant with the resonator frequency ω_{r}. The transmitted microwave is amplified several times (at low and at room temperature) before it is mixed to low frequency with a local oscillator (LO). The signal is then digitally acquired and post-processed by a computer using LabView software [17, 4]. For a detailed explanation of the experimantal setup see [23].

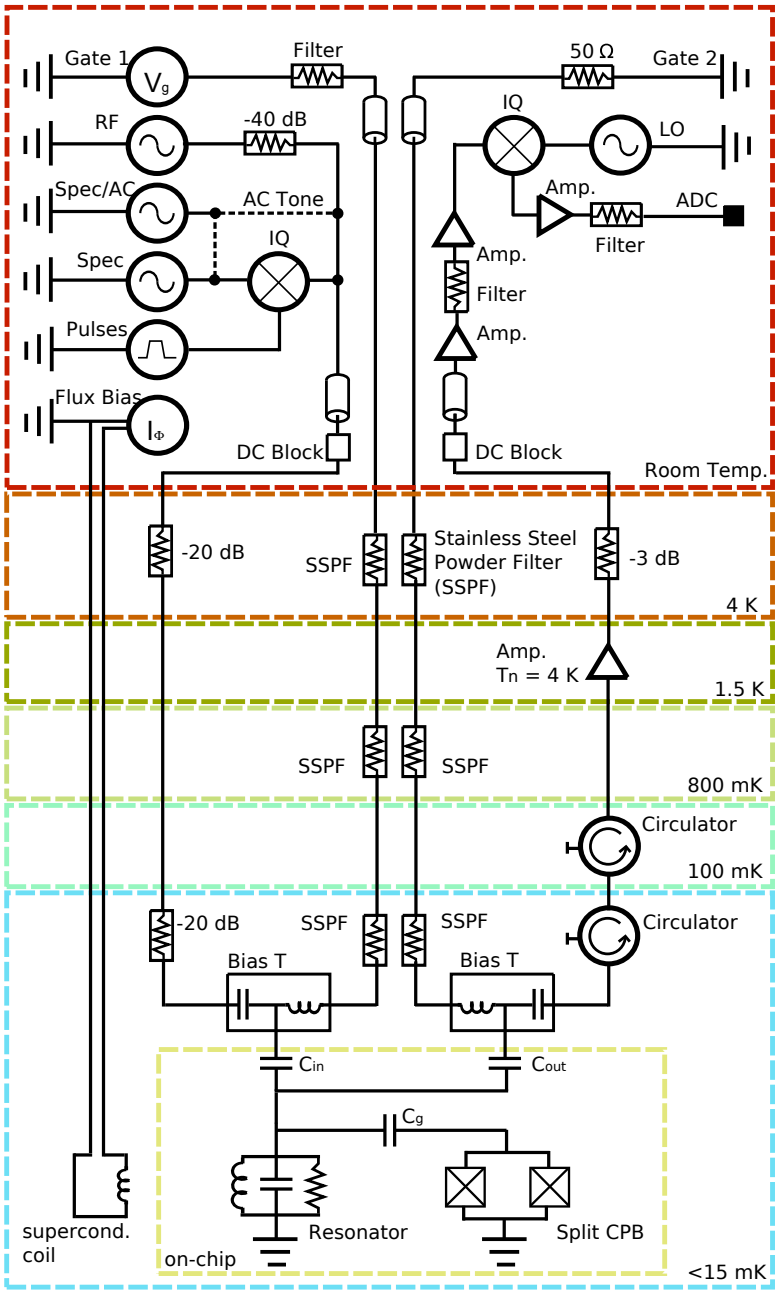

Figure 2.13: Schematic representation of the measurement and control setup. The top left section shows the instruments at room temperature used to generate the microwave and DC signals. The RF signals are modulated, filtered, attenuated and distributed via different coaxial lines and heat sinks at each temperature stage. The DC signal is low pass filtered with stainless steel powder filters and joined with the RF signal using a bias-tee. After interaction with the CPB, the transmitted signal gets amplified, filtered and downconverted with an IQ mixer to an IF signal before being digitally acquired [23].

3 Local qubit control

The main goal of this diploma thesis was the implementation of on chip gate lines which enable local qubit control. Local qubit control becomes important in multi qubit experiments. There one should be able to control the parameters of each qubit individually, without affecting the state of the other qubits or the resonator. Basically, there are three parameters, which can be controlled in a qubit, namely the qubit transition frequency ω_{01}, the number of excess charges n_g on the island (this isn't important for transmons, see subsection 2.2.3), and of course the qubit state $|\psi\rangle$.

This chapter reviews the mechanisms how the qubits can be controlled and explains how this has been implemented so far. The new ideas for the on-chip gate lines are also introduced, and will be discussed more deeply in the next chapters.

3.1 Control of the qubit state

While microwave irradiation of the cavity at its resonance frequency constitutes a measurement, irradiation close to the qubit's frequency can be used to coherently control the state of the qubit. As mentionned in subsection 2.4.3, the phase shift of the transmitted wave at the cavity frequency strongly depends on the state of the qubit and therefore the photons become entangled with the qubit. In the case of a large detuning between the drive frequency and the cavity frequency, the photons are mostly reflected with a phase shift which is independent of the state of the qubit.

By adding a term for the microwave drive to the Jaynes-Cummings Hamiltonian (2.19) one can obtain the effective one-qubit Hamiltonian in a frame rotating at the drive frequency $\omega_{\mu w}$ [1]:

$$\begin{aligned} H_{1q} &= \frac{\hbar}{2}\left(\omega_{\mathrm{a}} + 2\frac{g^2}{\Delta}\left(a^\dagger a + \frac{1}{2}\right) - \omega_{\mu w}\right)\sigma^z + \hbar\frac{g\varepsilon(t)}{\Delta}\sigma^x \\ &\quad + \hbar(\omega_{\mathrm{r}} - \omega_{\mu w})a^\dagger a + \hbar\varepsilon(t)(a^\dagger + a). \end{aligned} \tag{3.1}$$

Here $\varepsilon(t)$ denotes a measure of the drive amplitude. Choosing $\omega_{\mu w} = \omega_{\mathrm{a}} + (2n+1)g^2/\Delta$ will generate a rotation of the qubit around the x axis with Rabi frequency $g\varepsilon/\Delta$. For different drive frequencies, rotations around an arbitrary axis in the $x-z$ plane can be performed.

The implementation of the driving of the qubit transition is similar to the implementation of the measurement (cf. subsections 2.4.2 and 2.4.3), nameley the microwave signal couples via a small capacitor from the transmission line to the resonator and from there

it couples again capacitively to the island of the CPB, see also Fig. 2.13. As a consequence, photons that have a frequency which is detuned from the resonator frequency will be filtered and only a small amount of the drive signal applied will reach the CPB. Over the same cabling, but by applying a DC voltage rather than RF signals, the charge n_g on the island was controlled.

To control a qubit state locally one has to use a gate line that couples directly to the CPB and as little as possible to the resonator or the other qubits. A circuit diagram of such a gate line is shown in Fig. 3.1. Compared to the coupling via the resonator, the drive signals are not filtered by the cavity. This means on one side, that one can drive the qubit faster with the same power than via the resonator, but on the other side, a direct line offers also a direct decay channel for the qubit state.

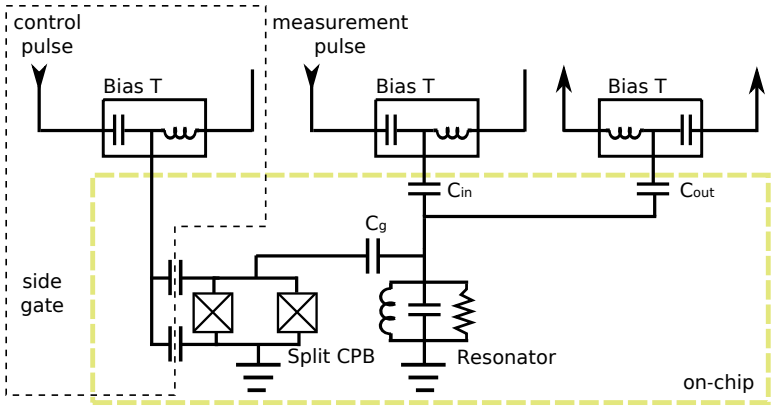

Figure 3.1: Circuit diagram of a gate line that allows to drive a qubit directly without affecting the resonator or other qubits.

3.2 Control of the qubit transition frequency

The qubit transition frequency can be calculated using the Hamiltonian (2.1). The exact solutions are functions containing Mathieu's characteristic values, but for the limits of a conventional CPB ($E_J/E_C \lesssim 1$) or a transmon ($E_J/E_C \gg 1$) one can give good approximations [19]. For a conventional CPB the transition energy near the sweet spot $n_g = 1/2$ is

$$E_{01}^{\mathrm{CPB}} = \sqrt{[4E_C(2n_g - 1)]^2 + E_J^2}. \tag{3.2}$$

The transition energy of a transmon can be approximated by

$$E_{01}^{\mathrm{Transmon}} = \sqrt{8E_J E_C}. \tag{3.3}$$

In both cases, the transition frequency strongly depends on E_J.

As seen in subsection 2.2.2 and Eq. (2.4), the effective Josephson energy is flux tunable in a split CPB. This means that by changing the magnetic flux through the SQUID loop

of the split Cooper pair box, one can tune the transition frequency of the qubit (see Fig. 3.2).

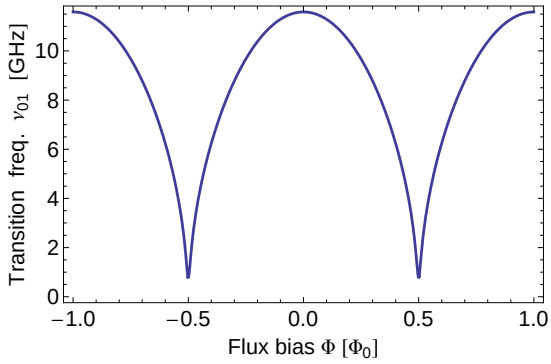

Figure 3.2: Qubit transition frequency ν_{01} as a function of the flux bias Φ/Φ_0 for a transmon with $E_J/h = 45$ GHz and $E_C/h = 400$ MHz.

In the present setup, the flux through the Cooper pair boxes is adjusted by an external coil (see Fig. 2.13). To control the flux through each CPB individually one has to use gate lines again. The current which comes from a current source can either be returned to the source or the line can be shorted such that the current flows in the groundplanes on the chip. The latter version has the advantage that one needs just one input port instead of an input and an output port on the chip. A circuit diagram of such a line is shown in Fig. 3.3.

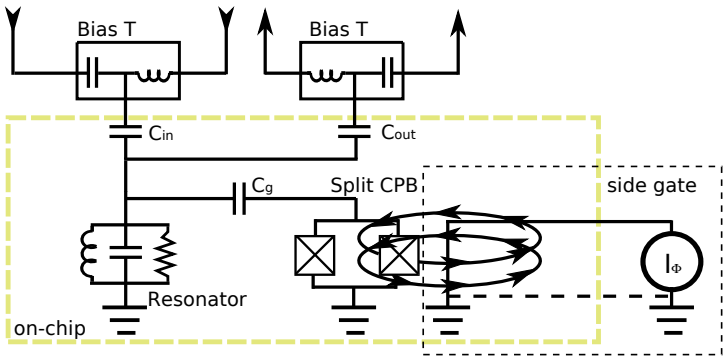

Figure 3.3: Circuit diagram of the flux gate line to change the flux in the SQUID loop of the split CPB. The current coming from a current source can either be returned to the source (dashed line) or lead to the ground on the chip.

4 Local drive and charge gate line

This chapter explains in more detail, how the final design of the local drive and charge gate line was chosen. The most straightforward approach for such a gate line is just a line like the resonator which couples directly to the CPB. This is a line with a characteristic impedance of 50 Ω with the same width as the resonator line.

The capacitances between the gate line and the parts of the Cooper pair box determines the coupling. These capacitances depend on the distance between the gate line and the reservoir of the CPB and the geometry of the CPB. Once the distance between the gate line and the resonator has been fixed, one can still increase the coupling by enlarging the reservoir and putting it nearer to the gate line. Putting the reservoir nearer to the gateline has two effects, namely the decay time T_1 will decrease and the Rabi frequency ν_{Rabi} will increase at fixed drive power.

Fig. 4.1 shows a model of the drive line. To be able to estimate the coupling strength and the decay time of a model, a formalism to calculate these values is developped in the following sections. This is needed to chose the optimal distance between the driveline and the reservoir.

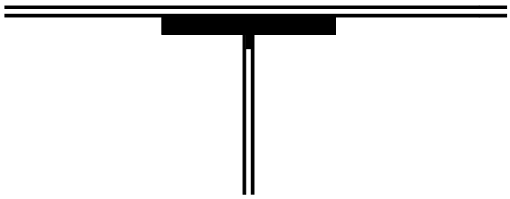

Figure 4.1: Design of the charge gate line. The white regions symbolize metal parts and the black regions substrate. The horizontal line on the top is the resonator, the big black square is a gap to put a transmon qubit in, and the vertical line is the drive line.

In section 4.1, a formula for T_1 is derived based on the two-state approximation. In section 4.2, a numerical solution is provided and compared with the two-state approximation. The voltage division for a Cooper pair box with a not grounded reservoir is derived in section 4.3. Sections 4.4 and 4.5 explain the estimation of the coupling g to the resonator and the expected Rabi frequency. At last the final design of the charge and drive line is presented in section 4.6.

4.1 Calculating the decay rate of a Cooper pair box due to coupling to an Ohmic environent

In the charge regime where $4E_C \gg E_J$ and considering just the two lowest charge states $|n=0\rangle$ and $|n=1\rangle$, the Hamiltonian of a Cooper pair box can be written in the following simple form:

$$H = -\frac{E_{\mathrm{el}}}{2}\sigma_z - \frac{E_J}{2}\sigma_x, \tag{4.1}$$

where $E_{\mathrm{el}} = 4E_C(1-2n_g)$ is the electrostatic energy and $E_J = E_{J,\max}\cos(\pi\Phi/\Phi_0)$ the Josephson energy. Note that this form is written in terms of the charge eigenstates.

In general, the ground and excited state of the qubit ($|g\rangle$, $|e\rangle$) do not correspond to eigenstates of the charge number operator but are given by $|g\rangle = \cos(\theta/2)|0\rangle + \sin(\theta/2)|1\rangle$ and $|e\rangle = -\sin(\theta/2)|0\rangle + \cos(\theta/2)|1\rangle$, where $\theta = \arctan(E_J/E_{\mathrm{el}})$ is a function of the gate voltage n_g and the flux Φ.

Let σ_z and σ_x denote the Pauli-matrices for the charge eigenstates and σ_z' and σ_x' these matrices for the qubit states. Then $\sigma_z = \cos(\theta)\sigma_z' - \sin(\theta)\sigma_x'$ and $\sigma_z' = \cos(\theta)\sigma_z + \sin(\theta)\sigma_x$. In terms of the qubit state basis, the Hamiltonian (4.1) can be written as

$$H = -\frac{E_{01}}{2}\sigma_z', \tag{4.2}$$

with $E_{01} = \hbar\omega_{01} = E_{\mathrm{el}}\cos\theta + E_J\sin\theta = E_{\mathrm{el}}\sqrt{1+\frac{E_J^2}{E_{\mathrm{el}}^2}}$ the energy level separation.

According to Fermi's Golden Rule, the decay rate of a two level system can be written as [24]:

$$\Gamma_\downarrow = \frac{A^2}{\hbar^2}S_f(\omega_{01}), \tag{4.3}$$

where A is a coupling constant, S_f ist the noise spectral density of some noise source and $\hbar\omega_{01}$ ist the energy level separation.

To calculate this rate, one has to find out the coupling constant A. In a two level system with a Hamiltonian like (4.2), one can describe the decay with an additional term $Af(t)\sigma_x$ in the Hamiltonian, where $f(t)$ is an amplitude that describes the noise source.

By writing the charge as a sum of a constant mean value and a time dependent perturbation, $n_g(t) = \overline{n}_g + \delta n_g(t)$, the Hamiltonian (4.1) can be written as

$$H = -\frac{E_{01}}{2}\sigma_z' + 4E_C\cos(\theta)\delta n_g(t)\sigma_z' - 4E_C\sin(\theta)\delta n_g(t)\sigma_x'. \tag{4.4}$$

To calculate the decay rate from $|e\rangle$ to $|g\rangle$, one has to find the coupling constant A of the perturbation in the σ_x' direction. In terms of gate voltage noise $V(t)$, the σ_x' perturbation term has the form $AV(t)\sigma_x'$. Comparing this expression with above equation and considering that $E_C = e^2/(2C_\Sigma)$ and $\delta n_g(t) = C_gV(t)/(2e)$, yields $A = e\beta\sin(\theta)$ with $\beta = C_g/C_\Sigma$.

The spectral voltage noise density is [24]

$$S_{\mathrm{V}}(\omega_{01}) = \frac{2\hbar\omega_{01}R}{1 - e^{\frac{-\hbar\omega}{k_B T}}}, \tag{4.5}$$

which gives in the low temperature limit $S_{\mathrm{V}}(\omega_{01}) = 2\hbar\omega_{01}R$. Combining all these equations gives:

$$T_1 = 1/\Gamma_{\downarrow} = \frac{1}{\beta^2 \sin^2\theta} \frac{R_K}{4\pi R\omega_{01}}, \tag{4.6}$$

where $R_K = h/e^2$ is the resistance quantum.

4.2 Numerical solutions of the decay times

The solution based on the two state approximation is a good approximation when E_J/E_C is small as in the case of a normal Cooper pair box. In this situation, the energy difference between the first and second excited state is much bigger than the energy difference between the ground and first excited state, which allows to neglect all higher states.

However, in the case of a transmon, the energy level separation becomes more symmetric with growing E_J/E_C and the energy level separation between the first and second excited state can even be slightly smaller than the level separation between the ground and first excited state [19]. In this case one can no longer use a two state approximation and has to consider many charge states.

The only way to do this is solving the Hamiltonian numerically. A *Mathematica* notebook which shows the calculation can be found in appendix A. It is based on a function which calculates the Eigenstates of the Hamiltonian, written by Alexandre Blais[1].

To understand the numerical solution, recall the electrostatic part of the CPB Hamiltonian (2.1)

$$H_{\mathrm{el}} = 4E_C(\hat{n} - n_g)^2, \tag{4.7}$$

which is the only part which depends on the gate charge n_g and contributes to a decay due to charge noise. For a small charge noise $n_g = \bar{n}_g + \delta n_g$ with $\delta n_g \ll \bar{n}_g$, one can perform a Taylor expansion up to first order

$$\hat{H}_{\mathrm{el}} \to \hat{H}_{el} + \delta n_g \left.\frac{\partial \hat{H}_{\mathrm{el}}}{\partial n_g}\right|_{\bar{n}_g} = \hat{H}_{el} - \delta n_g 8E_C(\hat{n} - \bar{n}_g). \tag{4.8}$$

According to Fermi's Golden Rule, the relaxation rate can be expressed as

$$\Gamma_1 = \frac{1}{T_1} = \frac{1}{\hbar^2} \left|\langle 1| - 8E_C(\hat{n} - \bar{n}_g)\,|0\rangle\right|^2 S_n(\omega_{01}), \tag{4.9}$$

[1] A. Blais, Département de Physique, Université de Sherbrooke, Sherbrooke, Québec J1K 2R1, Canada

where $S_n(\omega_{01}$ is the charge noise spectral density at the qubit transition frequency. This value can be expressed as a function of the voltage noise spectral density S_V (4.5):

$$S_n(\omega) = \left(\beta \frac{C_\Sigma}{2e}\right)^2 S_\mathrm{V}(\omega), \tag{4.10}$$

where C_Σ is the total capacitance of the island, e the unit charge, and β the voltage division.

To compare the numerically exact solution for the decay due to charge noise with the solution calculated using the two state approximation, the values for the decay time in dependence of the gate charge are plotted in Fig. 4.2. The numerical solution was computed in an 11-dimensional Hilbert space, incorporating the charge basis states from $|-5\rangle$ to $|5\rangle$. The red lines in the plots indicate the numerically exact solution and the blue lines are based on the two state approximation. Fig. 4.2 a) shows the calculations for a Cooper pair box and Fig. 4.2 b) the same calculation for a transmon. The parameters for these calculations are the ones in Tab. 4.1 in section 4.6. As one can see, the two state approximation is good for the CPB but cannot be used for transmons anymore.

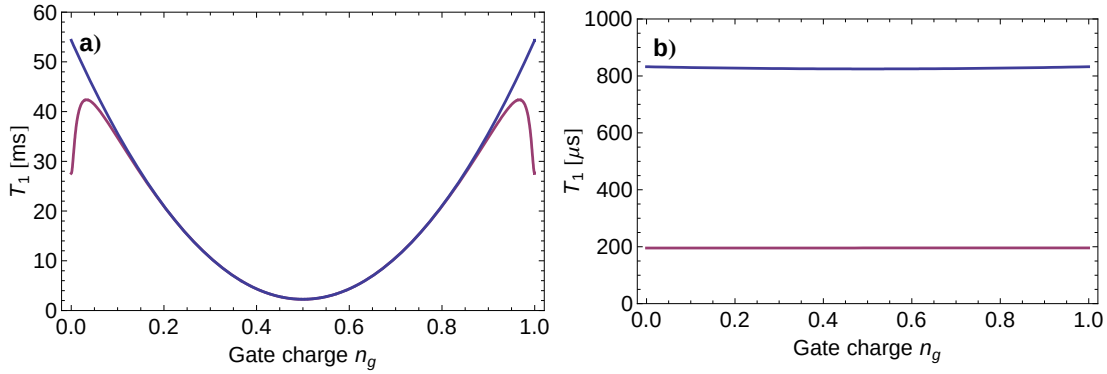

Figure 4.2: Decay time in dependence of gate charge. Comparison between numerically exact solution (red) and solution of the two state approximation (blue) in the case of a conventional Cooper pair box (a) and a transmon (b). The parameters used for these calculations are discussed in section 4.6 and Tab. 4.1.

4.3 Calculating the voltage division

In order to calculate the T_1 time, one needs to know the voltage division $\beta = V_j/V_g$. In the simple case illustrated in Fig. 4.3 this value is just equal to C_g/C_Σ where $C_\Sigma = C_g + C_J$.

This simple circuit describes the case of a conventional CPB whose reservoir is connected to the ground plane quite well. But in the case of a transmon the reservoir is not connected to the ground plane (see Fig. 2.6). Furthermore due to the geometry of

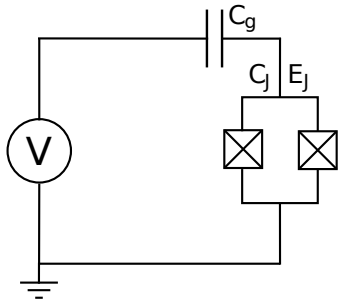

Figure 4.3: Circuit diagram of a simplified circuit, where the Cooper-pair box couples capacitively to a gateline.

the transmon, the island cannot be considered as coupled only to the gate. In a more realistic model, the coupling of the island and the reservoir to both, the ground and the gate has to be considered. Fig. 4.4a shows such a circuit and Fig. 4.4b shows a schematic of the Cooper-pair box in the resonator with a gateline. Note that the capacitances to the ground (C_{24}, C_{34}) are not just to one ground plane as in the figure, but are the sum of the capacitances to all grounding elements.

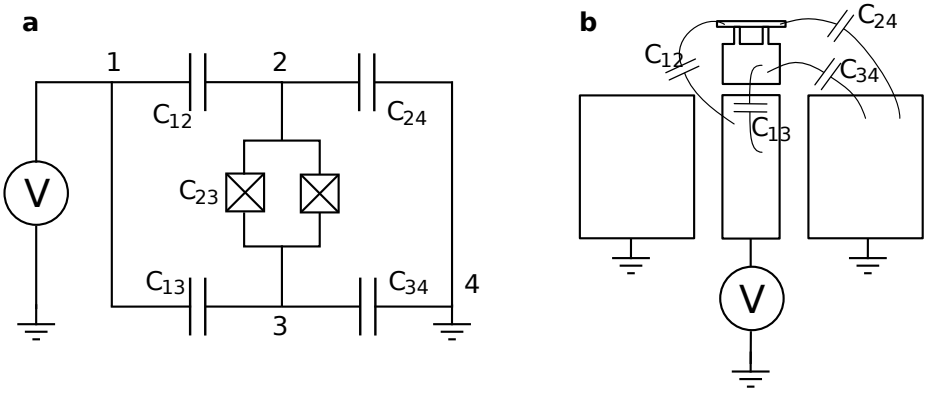

Figure 4.4: a) Circuit diagram of the more realistic circuit, where the island and the reservoir of the Cooper-pair box couple capacitively to ground and to the gateline. The numbers indicate islands, to which the island voltages V_i and charges q_i refer. b) Simplified schematic of the Cooper-pair box situated in the resonator near the gateline.

In this model, the calculation of the voltage division out of the given capacitances is more complicated. Assuming that these capacitances and the gate voltage are known, one can find the voltage across the Cooper-pair box as followings [17, p. 130 ff.]: Let $|C_{ij}|$ be the capacitance between node i and j of the circuit. One can define a capacitance

Matrix

$$C_{ij} = C_{ji} = -|C_{ij}|, i \neq j \tag{4.11}$$
$$C_{ii} = -\sum_{j \neq i} C_{ij}. \tag{4.12}$$

This capacitance matrix has the property that

$$\vec{q} = C \cdot \vec{v} \tag{4.13}$$

where $\vec{q}$ is a vector of island charges and $\vec{v}$ is a vector of island voltages. Writing down Eq. (4.13) explicitly as a sum gives:

$$q_i = \sum_j C_{ij} v_j. \tag{4.14}$$

If all the charges or all the voltages are known, it is easy to find the unknown quantities. Typically there are mixed conditions, with the charge on the box specified and the voltage on the gate specified. But since one knows for each island either the charge or the potential, one can rewrite this equation in the following form:

$$q_i = \sum_{j \leq i_0} C_{ij} v_j + \sum_{j > i_0} C_{ij} v_j, \tag{4.15}$$

where the enumeration is chosen such that for islands $i \leq i_0$, the charges q_i are known and for $i > i_0$ the potentials v_i are known. This equation can be rewritten as

$$q_i - \sum_{j > i_0} C_{ij} v_j = \sum_{j \leq i_0} C_{ij} v_j, \tag{4.16}$$

where all the unknown quantities are now on one side and can be determined.

In our case we assume that there is no initial charge on the islands, i.e. $q_2 = q_3 = 0$ and the voltages on the gates are $V_1 = V$, $V_4 = 0$. This leads to the following system of equations:

$$\begin{pmatrix} q_2 - C_{12} v_1 - C_{24} v_4 \\ q_3 - C_{13} v_1 - C_{34} v_4 \end{pmatrix} = \begin{pmatrix} C_{22} & C_{23} \\ C_{23} & C_{33} \end{pmatrix} \begin{pmatrix} v_2 \\ v_3 \end{pmatrix}. \tag{4.17}$$

These equations can be solved for v_2 and v_3 and hence the voltage division $\frac{v_3 - v_2}{V}$ can be calculated. The result is

$$\beta = \frac{C_{13} C_{24} - C_{12} C_{34}}{(C_{12} + C_{24})(C_{13} + C_{34}) + (C_{12} + C_{13} + C_{24} + C_{34}) C_{23}}. \tag{4.18}$$

4.4 Calculation of the coupling g to the resonator

Another important quantity is the atom-field coupling constant g of the qubit in the resonator. This coupling is determined by the following equation [19]:

$$\hbar g_{ij} = 2\beta e V^0_{\text{rms}} \langle i | \hat{n} | j \rangle, \tag{4.19}$$

where g_{ij} is the coupling between the ith and jth eigenstates of the CPB, β is the voltage division, e the elementary charge, $V^0_{\text{rms}} = \sqrt{\hbar\omega_r/2C_r}$ the root mean square voltage of the resonator field and $\langle i|\hat{n}|j\rangle$ the matrix element with $\hat{n}$ the number operator of the island charge.

In the case of a qubit, one has just to consider the coupling between the ground and the first excited state, i.e. $\langle 1|\hat{n}|0\rangle$. In the case of a normal CBP where E_J/E_C is small, this matrix element is approximately $\langle 1|\hat{n}|0\rangle \approx 0.5$, which gives the formula for the coupling in the CPB:

$$g = \frac{\beta e}{\hbar}\sqrt{\frac{\hbar\omega_r}{2C_r}}. \tag{4.20}$$

In the case of a transmon, where $E_J/E_C \approx 30 - 50$, the matrix element is asymptotically [19]

$$\langle 1|\hat{n}|0\rangle \approx \sqrt{\frac{1}{2}}\left(\frac{E_J}{8E_C}\right)^{1/4}, \tag{4.21}$$

and the coupling is calculated by

$$g = \frac{2\beta e}{\hbar}\sqrt{\frac{\hbar\omega_r}{2C_r}}\sqrt{\frac{1}{2}}\left(\frac{E_J}{8E_C}\right)^{1/4}. \tag{4.22}$$

To calculate the voltage division β, the same model as mentionned before was used, but instead of considering the capacitances to the gateline and the ground, the capacitances to the resonator and to ground has been used.

4.5 Calculation of the expected Rabi frequency

The Rabi frequency is characteristic for the strength of the coupling between the applied voltage and the qubit. It can be calculated in the same way as the coupling g but with the applied input voltage V_{inp} instead of the vacuum voltage fluctuations V^0_{rms}:

$$\omega_{\text{Rabi}} = \frac{2\beta e}{\hbar} V_{\text{inp}} \langle i|\hat{n}|j\rangle . \tag{4.23}$$

The maximum input voltage can be estimated by $V_{\text{inp}} = \sqrt{P_{max} Z_0}$, where P_{max} is the maximum power which can be put on the line and Z_0 is the impedance of the line which is typically $Z_0 = 50\ \Omega$. The maximum power on the line is determined by the maximum output power of the microwave source (~ 15 dBm) and the total attenuation on the way to the gate (~ -70 dB), this yields $P_{max} \approx 3$ nW.

The Rabi frequency depends linearly on β, while the decay time T_1 is proportional to $1/\beta^2$ (see Eqs. (4.6) and (4.9)). This means that if one changes the design of the reservoir, such that it is nearer to the gate such that the capacitances and β will increase, one gets a higher Rabi frequency but a lower decay time.

4.6 Final design of the charge/drive gate line

For the calculation of the estimated T_1 time one needs all the capacitances between the different parts of the circuit. These capacitances can be simulated with Maxwell® 3D. Simulations with different distances between the gate line and the gap for the transmon have been done (for a conventional CPB the distance between the gateline and the resonator line has been varied). From these simulation the final design with a distance between the gap and the gate line of 25 μm, as shown in Fig. 4.1, was chosen. For this distance, the simulated and calculated properties are shown in Tab. 4.1.

If one assumes a decay rate of $T_1 = 8$ μs for the qubit without the gate line, then the additional gate line with a 25 μm gap will reduce this T_1 less than 0.4 μs. This low influence to the T_1 and the fact that one doesn't want lower Rabi frequencies makes it reasonnable to chose this value.

		Conventional CPB	Transmon
C_{12}	[fF]	0.0016	0.140
C_{13}	[fF]	0.046	0.225
C_{24}	[fF]	0.410	50.0
C_{34}	[fF]	3.63	44.0
C_{23}	[fF]	4.0	30.0
E_J/h	[GHz]	3.7	15
ν_{01}	[GHz]	5.4	7.8
β		0.00073	0.00101
C_Σ	[fF]	4.37	5.33
E_C/d	[GHz]	4.43	0.36
T_1	[ms]	2.2	0.19
ν_{Rabi}	[MHz]	70	100

Table 4.1: This table shows the simulated capacitances for the two cases of the conventional CPB and the transmon, the assumed Josephson energy and qubit transition frequency, and the properties which were calculated out of these values: The voltage division β, the effective total capacity of the island C_Σ, the charging energy E_C, the decay time due to coupling to the gate line T_1, and the expected Rabi frequency ν_{Rabi}.

5 Flux gate line

A flux gate is a line passing near the split Cooper pair box, such that a current sent through the line induces a magnetic field in the loop of the CPB. This allows to control the effective E_J (see section 3.2). Generally one can think about two different types of lines. The first type is a line with two terminals, one for the source and one for the sink of the current as shown in Fig. 5.1. The second type has just one terminal for the current source and the line is shorted to ground on the chip. For this type, again two different design ideas were developped as shown in Fig. 5.2.

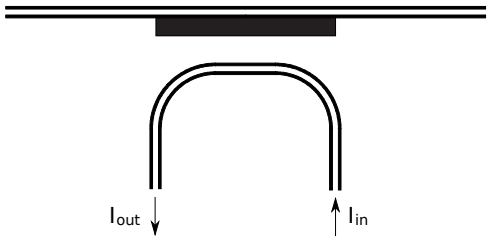

Figure 5.1: Design of the two-terminal flux line, passing by the resonator and the gap for the transmon qubit.

The one shown in Fig. 5.2 a) is refered to as "short" flux line. It was chosen because it is a simple design from which it is believed that the current flows symmetrically to both sides at the short and that the structure represents a close to ideal electrical short at the relevant frequencies. The design in Fig. 5.2 b) is denoted as "hockey-stick" flux line and it is supposed to give a higher magnetic flux, because all of the current flowing through it will contribute to the magnetic field and not just the half of it. However it is not clear what happens to the current at the end of the line. If a part of the current will flow back between the transmon gap and the line, this will produce a flux in the opposite direction that will reduce the effective flux through the SQUID loop of the CPB.

I addition to the capacitive coupling which influences the decay time, noise in the flux will couple to the Josephson term of the Hamiltonian (2.1) and contribute to the decay of the quantum state.

In section 5.1 the formalism to calculate the flux coupling and the thereby related decay time is developped.

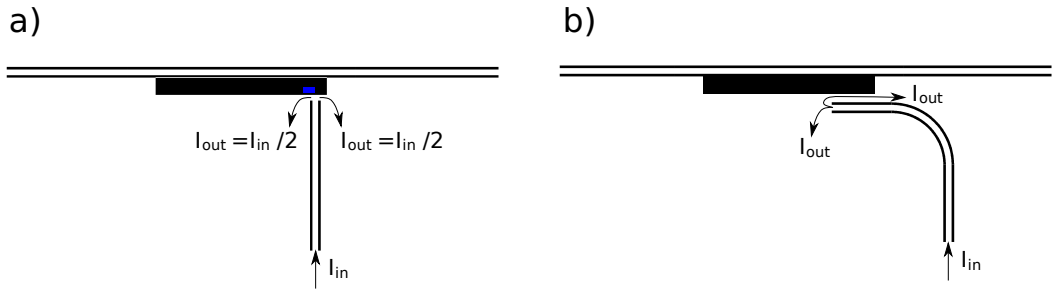

Figure 5.2: Designs of the shortened flux line. The arrows indicate the current flow. The blue box in a) is the place where the qubit loop should be placed to achieve maximum flux. The line a) is refered to as "short" flux line, while the line b) is refered to as "hockey-stick" flux line.

5.1 Calculating the decay rate due to flux noise

The additional flux lines allow to tune the Josephson coupling energy of a Cooper pair box or a transmon. But these gate lines offers also a channel for energy relaxation [19, 17, 25]. Instead of coupling via the voltage division to the electrostatic component of the Hamiltonian, it couples to the Josephson term via a magnetic inductance.

In this analysis, two mechanisms of flux coupling are considered. At first, there is the coupling between the SQUID loop and the flux line through the mutual inductance M; in addition, the entire transmon circuit couples to the flux line through a mutual inductance M' (cf. Fig. 5.3).

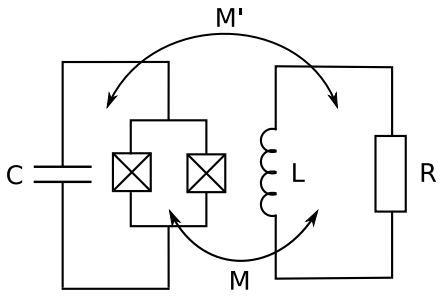

Figure 5.3: Model for the estimate of relaxation times due to flux coupling.

For the first mechanism, let's consider the Josephson term of the Hamiltonian, which can be written as:

$$\hat{H}_J = -E_{J\Sigma}\left[\cos(\pi\Phi/\Phi_0)\cos\hat{\varphi} + d\sin(\pi\Phi/\Phi_0)\sin\hat{\varphi}\right], \tag{5.1}$$

where $E_{J\Sigma} = E_{J1} + E_{J2}$ is the sum of the Josephson energies of the two junctions, $\hat{\varphi} = (\phi_1 + \phi_2)/2$ the effective phase difference and $d = (E_{J2} - E_{J1})/E_{J\Sigma}$ the junction asymmetry.

If the noise $\delta\Phi$ is much smaller than the external flux $\Phi_{\text{ext.}}$, one can perform a Taylor expansion of the Josephson Hamiltonian (5.1):

$$\hat{H}_J \longrightarrow \hat{H}_J + \delta\Phi\hat{A}, \tag{5.2}$$

where

$$\begin{aligned} \hat{A} &= \left.\frac{\partial\hat{H}_J}{\partial\Phi}\right|_{\Phi_{\text{ext.}}} \\ &= E_{J\Sigma}\frac{\pi}{\Phi_0}\left[\sin\left(\frac{\pi\Phi_{\text{ext.}}}{\Phi_0}\right)\cos\hat{\varphi} - d\cos\left(\frac{\pi\Phi_{\text{ext.}}}{\Phi_0}\right)\sin\hat{\varphi}\right]. \end{aligned} \tag{5.3}$$

According to Fermi's golden rule the decay rate due to flux coupling is

$$\Gamma_1 = \frac{1}{\hbar^2}\left|\langle e|\,\hat{A}\,|g\rangle\right|^2 S_\Phi(\omega_{01}). \tag{5.4}$$

The flux noise spectral density can be expressed with the current noise and the mutual inductance:

$$S_\Phi(\omega) = M^2 S_{\text{I}}(\omega) = M^2\frac{2\hbar\omega}{R}\frac{1}{1-e^{\frac{-\hbar\omega}{k_{\text{B}}T}}}. \tag{5.5}$$

Using a two-state approximation, the Hamiltonian (2.1) can be solved algebraically and Eq. (5.4) can be expressed as follows:

$$\begin{aligned} &\Gamma_1 = \frac{\pi^2 M^2 S_{\text{I}}(\omega)}{\hbar^2\Phi_0^2} \\ &\cdot\frac{E_J^2\pi^2\left(d^2E_J^2 + 8\left(1+d^2\right)E_C^2(1-2n_g)^2 + 8\left(-1+d^2\right)E_C^2(1-2n_g)^2\cos\left[\frac{2\pi\Phi}{\Phi_0}\right]\right)}{2\Phi_0^2\left(\left(1+d^2\right)E_J^2 + 32E_C^2(1-2n_g)^2 - \left(-1+d^2\right)E_J^2\cos\left[\frac{2\pi\Phi}{\Phi_0}\right]\right)}. \end{aligned} \tag{5.6}$$

For the second mechanism, one can model the transmon as a simple LC oscillator with $L \approx \hbar^2/4e^2E_J$ and $C \approx e^2/2E_C$. Assuming that the charge oscillates classically with the frequency $\omega = \sqrt{LC}$ and that the energy stored is of the order of $\hbar\omega$, one obtains for the charge $Q(t) = Q_0\cos\omega t$ with $Q_0 = \sqrt{2C\hbar\omega}$ and for the current $I(t) = -I_0\sin\omega t$ with $I_0 = \omega\sqrt{2C\hbar\omega}$. The thereby induced voltage is $V_{\text{ind}}(t) = V_0\sin\omega t$ with $V_0 = M'\omega^2\sqrt{2C\hbar\omega}$. The environmetal impedance $R \sim 50\ \Omega$ will dissipate the average power $P = V_0^2/2R$. This leads to the following estimate:

$$T_1 \simeq \frac{\hbar\omega}{P} = \frac{RL^2C}{M'}. \tag{5.7}$$

5.1.1 Numerical solution

As already mentionned, the two state approximation is not valid in the case of a transmon qubit. A numerical solution can be provided in exactly the same way as described in section 4.2, but with the expressions (5.3) and (5.4) instead of (4.8) and (4.9).

Fig. 5.4 shows the comparison between the calculated T_1 times with the formula (5.6) and numerically considering 11 charge states as a basis (charge states from $|-5\rangle$ to $|5\rangle$). With the parameters discussed in section 5.2, the calculated decay times for the conventional CPB in the two models match exactly, but for the transmon one can see a deviation between the numerical solution and the two state approximation.

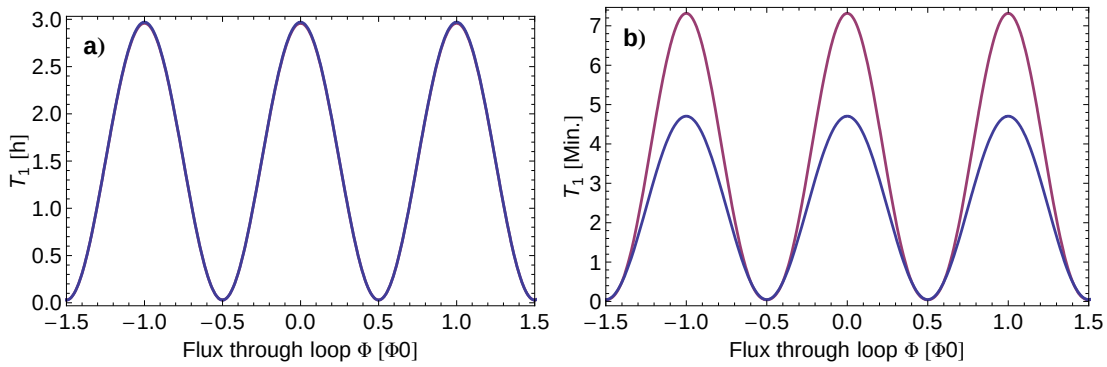

Figure 5.4: Decay time T_1 in dependence of flux through the SQUID loop. Comparison between numerically exact solution (red) and solution of the two state approximation (blue) in the case of a conventional Cooper pair box (a) and a transmon (b). The parameters used for these calculations are disussed in section 5.2 and Tab. 5.1.

5.2 Final designs for the flux gate lines

For the two-terminal flux line, one can estimate the effects to the decay rate due to capacitive coupling in the same way as for the gateline (cf. section 4.6). For the line shown in Fig. 5.1, with a distance of 50 μm between the gap and the line, this gives a decay rate of $T_1 \approx 450$ μs.

For the shorted flux lines, the capacitances cannot be taken from an electrostatical simulation as Maxwell® 3D does, because it treats the line also as grounded when it is connected to the ground. To estimate the capacitance from the island and the reservoir to the shortened lines, a Microwave Office® simulation was done to calculate the transmission. The transmission at 7 GHz was compared to a capacitor with the same transmission as calculated, and this capacitance was taken for further analysis. The capacitances to ground were taken from electrostatic simulations.

For the capacitive coupling between a transmon qubit and a hockey stick type flux line these simulations give $T_1 \approx 52$ ms and for the "short" type the decay rate is many seconds.

To calculate the relaxation due to flux coupling, one has to estimate the mutual inductance between the CPB and the gate line. To do this, magnetostatic simulations with Maxwell® 3D have been done. At a SQUID loop size of 4 μm^2 which is positionned

such that the flux through it is maximized, these simulations give for the short line a mutual inductance of $M \sim 2\ \Phi_0/\mathrm{A}$ and for the 2-port and the "hockey-stick" line a mutual inductance of $M \sim 5-7\ \Phi_0/\mathrm{A}$, which leads to a non-relevant contribution to the decay. But this means also, that the current needed for the change of the flux by one flux quantum is $140-500$ mA. The fact that one is able to control the whole qubit frequency range with half a flux quantum (see section 3.2) reduces the needed current by a factor of two. In addition, the "hockey-stick" and the two-port flux line generate a field in a longer section, which allows to design the SQUID loop larger, such that one could increase the mutual inductance by the design of the Cooper pair box.

The magnetostatic simulations in Maxwell® 3D cannot simulate superconducting materials, only ideal conductors. This could probably give wrong numbers for the mutual inductance, as the magnetic behaviour of superconductors and ideal conductors is different. Due to the Meissner-Ochsenfeld effect which expels a magnetic flux from the superconductor, the magnetic field in the loop (and therefore the flux through it) could be higher than simulated.

		Conventional CPB	Transmon
E_J/h	[GHz]	3.7	15
E_C/d	[GHz]	4.4	0.36
ν_{01}	[GHz]	5.4	7.8
M	[Φ_0/A]	0.00073	0.00101
T_1	[s]	> 2	> 50

Table 5.1: This table shows the the assumed Josephson energy, charging energy, and qubit transition frequency, the simulated mutual inductance M, and the calculated decay time at an external field $\Phi = 0.5\Phi_0$.

6 Design of the cabling for the new charge and flux gate lines

To make use of the new charge and flux gate lines on the resonator chip, additional wires for the pulses have to be added to the dilution refrigerator.

The implementation of the additional wiring is guided by the present wiring which allows to apply a DC bias voltage and microwave pulses to the resonator, see Fig. 2.13 and Ref. [23]. For the input and the output of the resonator, there are for each case two semi-rigid coaxial cables going down the cryostat, a DC line and an RF line. The signals of the two lines are combined at base temperature with a bias tee.

The reason why there are two different lines for DC and RF is, that one needs a good filtering to prevent thermal noise from disturbing the measurement and the qubit state. Noise at the qubit transition frequency will contribute to energy relaxation while low frequency noise far below the transition frequency contributes to the dephasing. Therefore the DC line has to be filtered with a low pass filter that eliminates any high frequencies. This can be achieved with stainless steel powder filters at different temperature stages. These devices serve as low pass filters which attenuate thermal RF noise very effectively. But this effective filtering of RF signals is the reason why one can not apply short control pulses on a DC line and therefore needs an additional RF lines.

The noise on the RF lines can be reduced by generating signals with a relatively high power and attenuating them together with the noise. According to Ref. [23], a power of ~ -145 dBm is sufficient for performing measurements, and ~ -60 dBm are appropriate to drive transitions in the qubit. Therefore a total attenuation on the RF lines of ~ 60 to 100 dB, which corresponds to a factor of 10^6 to 10^{10} of attenuation, can be implemented without limiting the measurement and drive ability.

For the new gate lines, one needs also a DC and an RF line. For the charge gates, the requirements are very similar to those for the current lines for the resonator. For the flux lines, one has to think more carefully about the implementation, because some additional requirements need to be fulfilled. To induce a magnetic field, one needs current, not voltage, this could cause e.g. the problem that too much power is dissipated in resistive elements at base temperature, which would heat up the cryostat.

In this section, different components and their possible usage for the new cabling are analysed.

6.1 Bias tee

A bias tee is a device which combines a DC signal with an RF signal. A circuit diagram is shown in Fig. 6.1. The capacitor C_1 prevents the DC signal from going to the RF

input while the inductor L prevents the microwave signal from going to the DC input.

The bias tees used to combine the DC bias voltage with the RF control and measurement pulses (see section 3.1) are of type K250 by *Anritsu*. Due to the device specifications they should have an RF frequency range of 0.1 to 40 GHz. This means that on can apply pulses of at maximum 10 ns length on the RF input. There were no specifications available for the bandwidth on the DC side. To check what pulses one could apply on the DC input, the transmission spectrum of the bias tee was measured with a network analyzer and the output of the bias tee was measured for different pulses and both DC and RF inputs.

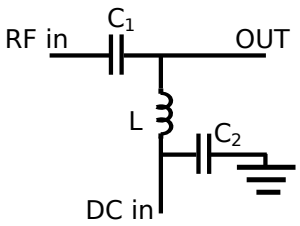

Figure 6.1: Circuit diagram of a bias tee. An RF signal is combined with a DC signal.

Fig. 6.2 shows the transmission between the RF input and the output of the bias tee (blue). The red curve shows the calculated insertion loss for the parameters that reproduce the pulseshapes accurately (see below), the The 3 dB point is at 9.2 MHz and according to this data it seems, that one could use the bias tee for lower frequencies than the specified 100 MHz. To check that, one can examine how an applied pulse looks at the output.

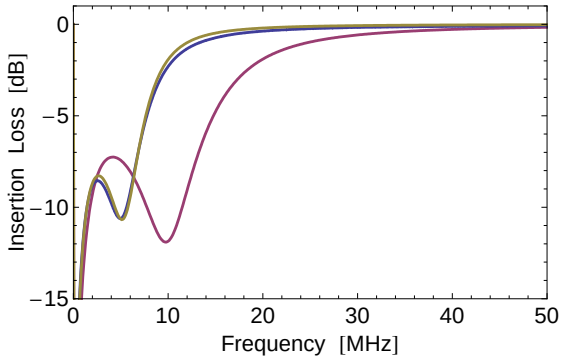

Figure 6.2: Measured insertion loss (blue line) between the RF input and the output of the bias tee K250, and calculated insertion loss for the parameters that optimally reproduce the measured pulse shapes (red line) and insertion loss curve (yellow line), respectively.

Fig. 6.3 shows the 100 ns square pulse, which was applied to the RF input, the response

at the output of the bias tee, and the output when a 10 ns square pulse is applied to the RF input. The red and yellow lines show the calculated pulse shapes for different parameters.

One can see that square pulses longer than 10 ns are not transmitted reasonably on the RF line.

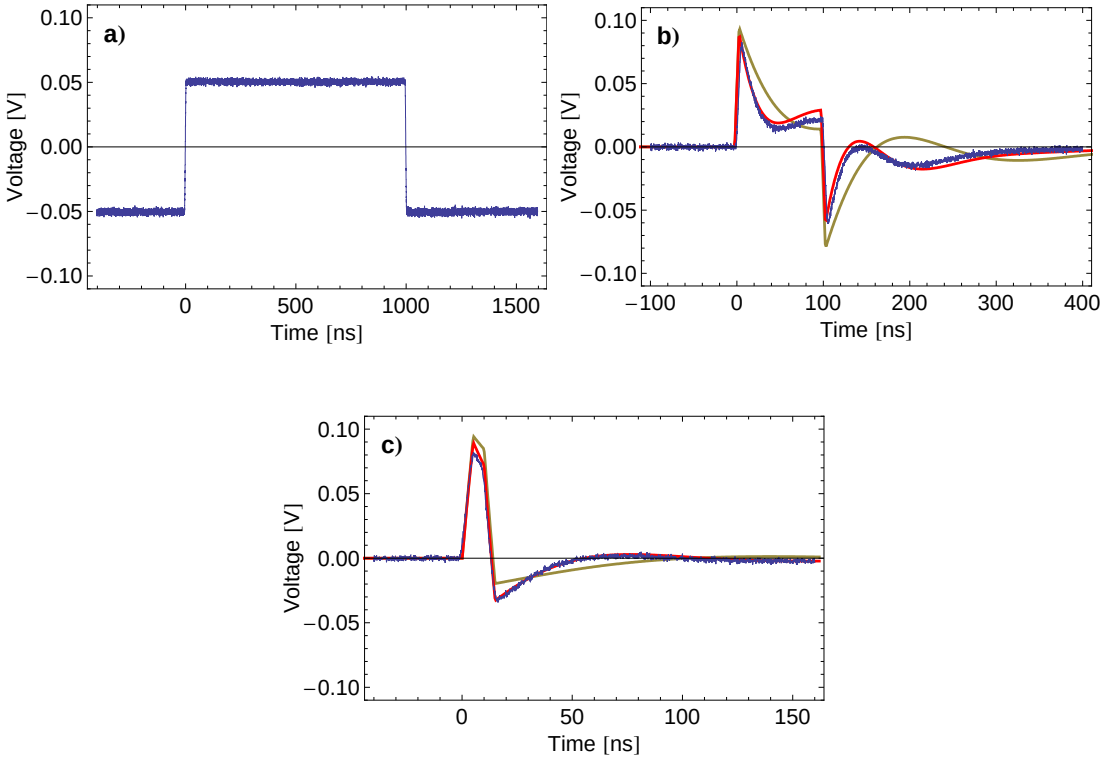

Figure 6.3: a): Pulse of 100 ns length as it is generated by the waveform generator. b,c): Measurement (blue) and simulation (red, yellow) of the output of the bias tee when a 100 ns (b) and a 10 ns (c) pulse is applied at the RF input.

To check the minimum length of a square pulse that can be transmitted through the DC input, similar measurements are done. The measurements of the transmission from the DC input to the output is shown in Fig. 6.4. The 3 dB point is at 3.5 MHz, which corresponds to a pulse length of $\sim$ 290 ns.

Fig. 6.5 shows the measuerment of the output when a 1 μs pulse and a 100 ns pulse is applied at the DC input. In the first case, one can see that it is still a square pulse, but the time needed to reach a constant level is on the order of 200 ns. The 100 ns pulse isn't anymore a square pulse but could probably still used in experiments.

Neverthless, square pulses between 10 ns and 100 ns cannot be produced, which probably will be needed in some experiments. This is the reason, why new bias tees are

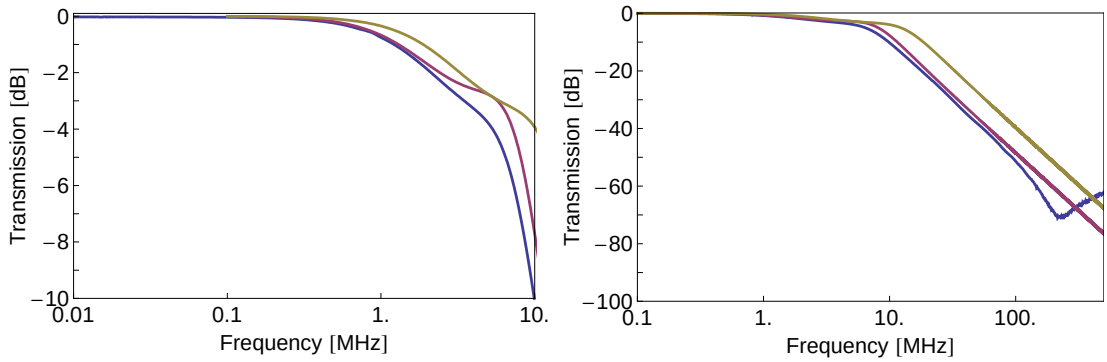

Figure 6.4: Blue: Measured transmission between the DC input and the output of the bias tee K250. Red, yellow: Calculated values for the parameters that optimally reproduce the measured pulse shapes (red) or the insertion loss curve (yellow).

needed with a lower boundary of the bandwitdth. A possible candidate is the model K251 of the same manufacturer which has an RF bandwidth from 50 kHz to 40 GHz. This should allow pulses up to a length of 20 μs on the RF input. For the DC side, the 3 dB point is at 23 kHz, which corresponds to a pulse length of 43 μs.

In order to estimate the effect from the type K251 bias tee on the pulses, one can estimate capacitances and an inductance which reproduce the insertion loss curve and calculate the pulse shapes. The estimation can be done with Microwave Office® by simulating the bias tee and adjusting the parameters until it matches the known data. To calculate the pulse shape, the Fourier transformed square pulse is multiplied with the filter function and transformed back into the time domain again.

To check whether this method is reliable, one can calculate the same for the K250 bias

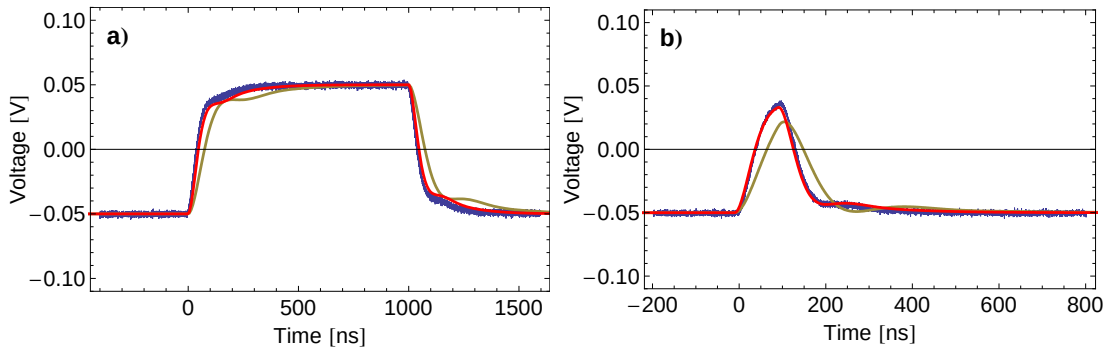

Figure 6.5: a): Measured (blue) and calculated (red) output of the bias tee when a 1 μs pulse is applied at the DC input. b): Output when a 100 ns pulse is applied.

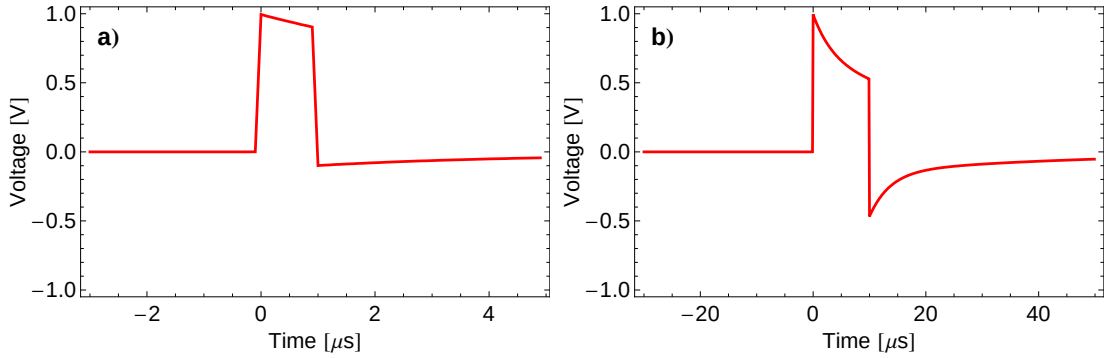

Figure 6.6: a): Calculated output of the bias tee K251 when a 1 μs pulse is applied at the RF input. b): Calculated output of the bias tee K251 when a 10 μs pulse is applied at the RF input.

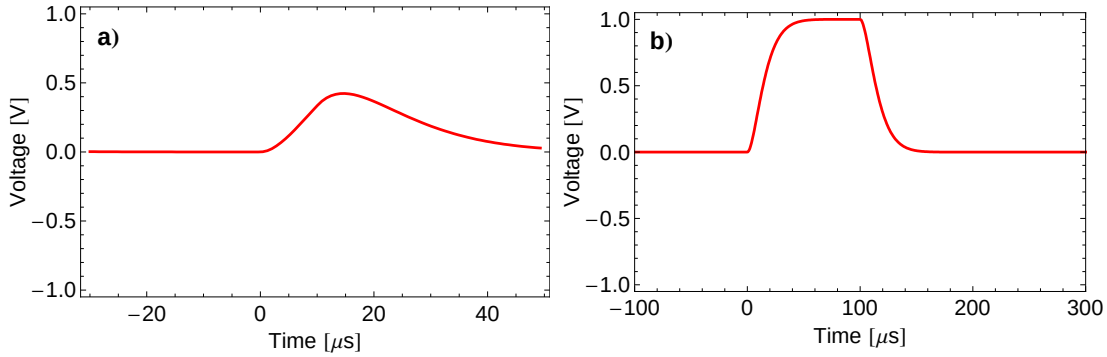

Figure 6.7: a): Calculated output of the bias tee K251 when a 10 μs pulse is applied at the DC input. b): Calculated output of the bias tee K251 when a 100 μs pulse is applied at the DC input.

tee and compare the results with the measured data. If the parameters are optimized such that the calculated insertion loss on both sides (DC and RF) is optimally reproduced ($C_1 = 0.9$ nF, $C_2 = 1.1$ nF, $L = 750$ nH), the pulse shapes are not reproduced very accurately (cf. Figs. 6.2 to 6.5, yellow plots). On the other side, if the parameters are adjusted such that the pulse shapes are optimally reproduced ($C_1 = 0.7$ nF, $C_2 = 0.7$ nF, $L = 350$ nH), the calculated insertion loss deviates from the measured one (cf. Figs. 6.2 to 6.5, red plots).

The fact that the pulse shapes and the insertion loss curves can be reproduced very well shows that the model used for the calculations is good (simpler models with just one capacitor don't show certain characteristics in the pulse shapes as well as in the insertion

loss curves). Nevertheless, the set of parameters that reproduce the best values should be the same for both cases and this discrepancy is not yet clear.

The estimation for values that reproduce the known data of the K251 bias tee are $C_1 = 270$ nF, $C_2 = 0.7$ nF, $L = 135$ μH. The calculated output for a 1 μs and a 10 μs pulse applied at the RF input are shown in Fig. 6.6. According to this data, square pulses up to 1 μs should be possible on the RF side. The results for the DC side are shown in Fig. 6.7. Further simulations show, that the maximum pulse length which gives a reasonable result is around 50 μs.

Tab. 6.1 shows the approximate limits for the pulse length for the K250 and the K251 bias tee which are estimated by the previous analysis.

	Longest square pulse on the RF side	shortest square pulse on the DC side
K 250	10 ns	100 ns
K 251	1 μs	50 μs

Table 6.1: Approximate limits for the current (K250) and the new (K251) bias tee.

6.2 Stainless steel powder filters

The stainless steel powder filters (SSPF) [26] are a further development of the copper powder filters [27]. The filters used to on the DC bias lines to adjust the charge on the island of the CPB are made with a constantan wire wound into a coil inside a copper mount which was filled with stainless steel powder type 316-L, -325 mesh by *Alfa Aesar* and STYCAST 1266 glue (see Fig. 6.10 and Ref. [23]). The problem with these filters is, that they have a DC resistance of about 10 Ω. When a flux bias is applied in the range of 1 mA, this gives a powerdissipation in the filter of 10 μW which clearly exceeds the cooling power the lowest temperature stage ($\sim$ 5 μW).

To reduce the power dissipation two new SSPF are constructed, one with a copper wire and one with a superconducting niobium wire. Both wires have a length of ca. 70 cm. The diameter of the copper wire is 0.2 mm and for the superconducting wire it's 0.1 mm.

Their attenuation was measured in a dipstick measurement in liquid helium with an *Advantest* R3753BH network analyzer for low frequencies (5 Hz - 100 MHz) and a *Rhode & Schwarz* ZVK network analyzer for high frequencies (10 MHz - 40 GHz). Fig. 6.8 shows the result of these measurements compared to filter with constantan wire.

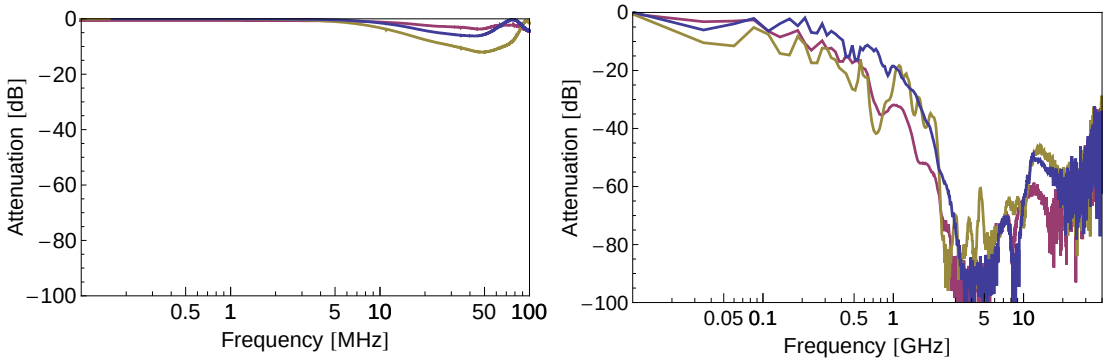

Figure 6.8: Attenuation of the copper wire filter (blue) and the niobium wire filter (yellow) compared to one with constantan wire (red).

At low frequencies, the filters show a peak at $\sim 70 - 100$ MHz, where the attenuation is very weak. At higher frequencies, the filters show an increase of the attenuation up to 100 dB at approximateley 2 GHz. In the range of ~ 2 to 10 GHz, the attenuation is rather good (more than 60 dB) but shows a lot of peaks and not the desired smooth behaviour. Above 20 GHz, one can see only the noise floor of the network analyzer, which means that the attenuation is very high in this region.

To improve the low pass filter properties further, one can combine the filter with a low-pass pi-filter. This should lead to a steeper increase of the attenuation at the cut-off frequency, which can also be adjusted [28]. The new filter is realised by soldering a surface mount type 0805 capacitor at the inside of each press-fit SMA connector, such that the capacitance lies between the center pin conductor and the ground.

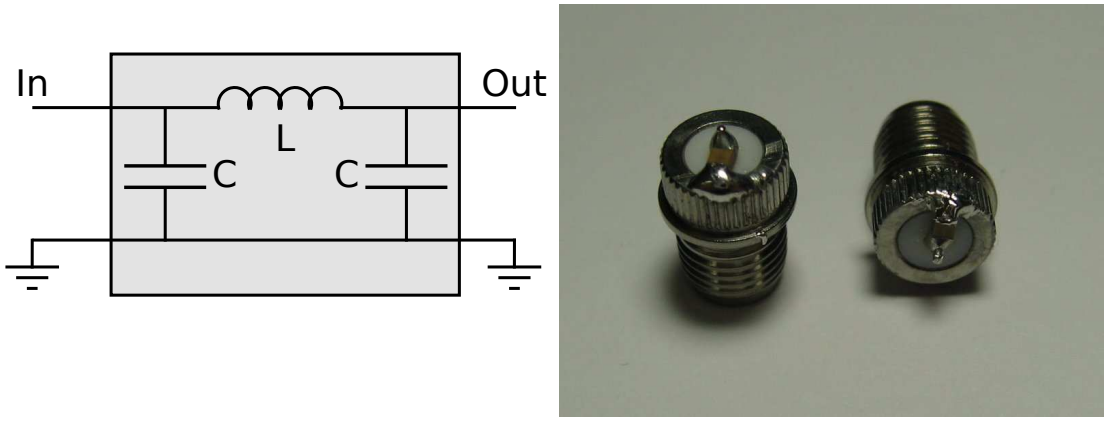

Figure 6.9: Left: Schematic of the SSPF with additional capacitances. Right: Photo of the press fit SMA connector with soldered capacitor.

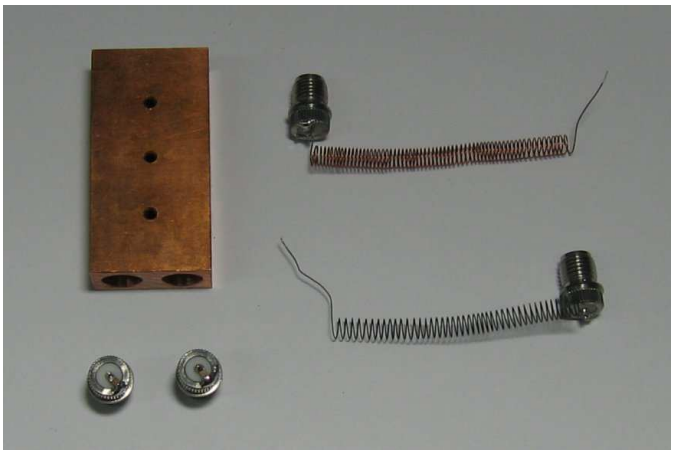

Figure 6.10: Different parts of the powder filter: The copper mount, copper and constantan wires wound into a coil with and soldered to a press-fit SMA connector with an additional capacitance soldered between the center pin and the ground.

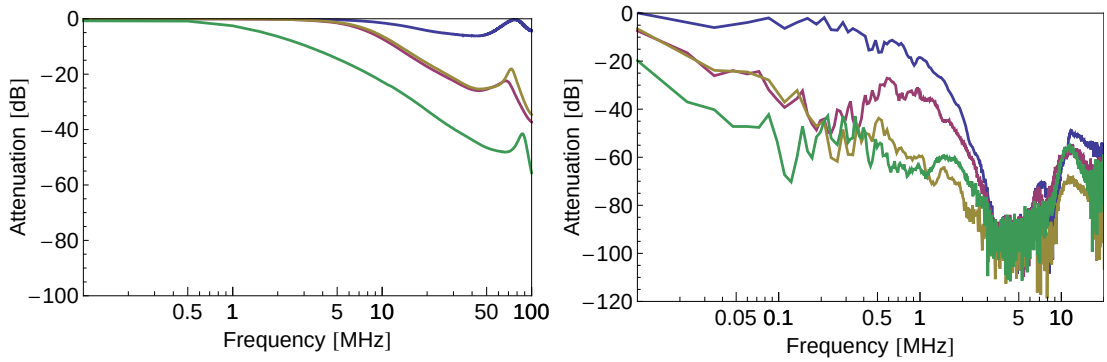

Figure 6.11: Attenuation of the copper wire filter with capacitances of $C = 10$ nF (red), $C = 50$ nF (yellow), $C = 100$ nF (green), compared to a conventional copper wire SSPF (blue).

The measurend attenuation of such filters for three different capacitances ($C = 10$ nF, $C = 50$ nF and $C = 100$ nF) is shown in Fig. 6.11. In the low frequency region a clear improvement is observed. The peaks at $70 - 90$ MHz are now much lower. In the 10 nF and the 50 nF filter they are around -20 dB and the 3 dB point is around 7 MHz. In the 100 nF filter the peak has its maximum at -40 dB and the 3 dB point is at about 1 MHz.

6.3 Attenuator configuration

To reduce the noise on the RF-lines, one can use attenuators. For the RF lines that couple to the resonator, there are two 20 dB attenuators per line, one at 4 K and one at base temperature ($\sim$ 20 mK). These values have been chosen such that the noise which comes from higher temperature stages is attenuated to the same level as the noise which is generated at the corresponding temperature stage.

Attenuators are passive resistive elements which are constructed of resistors. One common form is called "tee attenuator" (this is also the form of the currently used attenuators), its schematic is shown in Fig. 6.12.

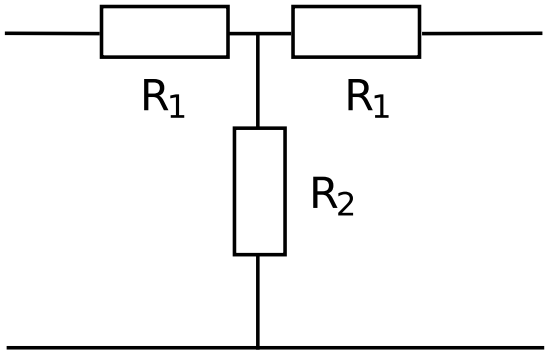

Figure 6.12: Schematic of a tee attenuator

As a resistive element, an attenuator dissipates power which is emitted to the environment as heat. This power can be calculated from the input voltage:

$$P_{\mathrm{dis}} = (V_{\mathrm{in}}^2 - 10^{-x\ \mathrm{dB}} V_{\mathrm{in}}^2)/Z_0,$$

where V_{in} is the input voltage, Z_0 the characteristic impedance of the system and x the attenuation in dB.

6.3.1 Flux lines

The problem with using the configuration which is designed to apply drive and measurement pulses for flux lines is, that the current needed for the magnetic field can lead to a power dissipation in the attenuators that is higher than the cooling power at the corresponding temperature stage.

At the lowest temperature stage, the cooling power is $\sim 5\ \mu$W. The power dissipateted by a single attenuator should therefore not be higher than 1 μW. From the attenuation and a given maximum power dissipation, one can calculate the maximum output voltage. For a 20 dB attenuator with 1 μW power dissipation this gives 710 μV, which gives a maximum current of 28 μA. But to change the flux by one flux quantum $\Phi_0 = \frac{h}{2e}$, one needs a current of $\sim$ 30 mA (for a 4×4 μm SQUID loop and an average field per

Attenuator configuration		P_{dis} [μW]	I_{out} [mA]	T_1 at 30 Φ_0/A	T_1 at 100 Φ_0/A
300 K	–	0	5.0	1.3 s	120 ms
4 K	10 dB	1125	1.58		
800 mK	20 dB	124	0.16		
20 mK	–	0	0.16		
300 K	–	0	5.0	480 ms	43 ms
4 K	10 dB	1125	1.58		
800 mK	10 dB	113	0.5		
20 mK	–	0	0.5		

Table 6.2: Calculated decay rates due to flux coupling for different attenuator configurations and different mutual inductances.

applied current of 0.004 T/A, taken form a Maxwell® 3D simulation). For this reason one cannot have a 20 dB attenuator at base temperature.

Calculations showed, that it is possible to still have high decay times by putting the attenuator to a different temperature level. The calculated decay rates for different attenuator configurations and different mutual inductances are shown in Tab. 6.2. The values are calculated at for a flux of $\Phi = 0.5\ \Phi_0$, which gives the longest decay rate. For $\Phi = 0$, the value decreases about two orders of magnitude.

6.3.2 Charge/drive lines

The calculations of the decay rate for the charge gate lines for different attenuator configurations is shown in Tab. 6.3. One can see, that one can not use the same configuration as for the flux lines without a large increase in the decay rate. An attenuator at 20 mK seems necessary for the charge gate lines.

Another limiting factor is the maximum output power of the microwave generator. This value determines the maximum available power at base temperature at a given attenuator configuration. The currently used microwave generators have a maximum output power of 40 dBm which corresponds to a voltage of 10 V. To give reasonable estimates for this number one has to consider the attenuation of the cables more detailed, which isn't done for low temperatures yet.

Neglecting the attenuation of the cables, the maximum voltage at base temperature can be 300 mV for the 20/10 configuration and 1 V for the 10/10 configuration.

Attenuator configuration		T_1 at 25 μm	T_1 at 1 μm
20 mK	–		
800 mK	20 dB	160 μs	1.4 μs
4 K	10 dB		
20 mK	–		
800 mK	10 dB	58 μs	0.5 μs
4 K	10 dB		
20 mK	10 dB		
800 mK	10 dB	510 μs	4.4 μs
4 K	20 dB		
20 mK	20 dB		
800 mK	10 dB	715 μs	6.2 μs
4 K	20 dB		

Table 6.3: Calculated decay rates due to coupling to the charge gate lines for different attenuator configurations. The distances indicate the distance between the bottom of the transmon and the gate line.

6.4 Suggested configuration

Bias tee With the present bias tees, one can not apply DC-pulses with a length between 10 ns and 100 ns. Therefore new bias tees with a larger frequency range on the RF side are needed.

SSPF Stainless steel powder filters with copper wire are definitely needed for the flux lines. About the exact values of the capacitances has to be investigated more.

Attenuators A good configuration for the attenuators is 10 dB at 4 K and 10 or 20 dB at 800 mK for the flux lines and 20 dB at 4 K, 10 dB at 800 mK and 20 dB at 20 mK for the charge lines.

7 Resonator characterization and cross coupling

7.1 Resonator design

The chips with the resonators and the side gates have been designed in *Mathematica*. For each part of the chip, like the resonator, the in- and output capacitances, the different types of side gates etc., a *Mathematica*-function was written which allows to vary certain characteristic parameters (e. g. the length of the resonator, the structure of the capacitances etc.). These functions can all be combined in a modular way to easily generate the desired designs with only a few lines of code.

In total, about 90 different chips with 30 different designs have been fabricated. The designs vary in the fundamental frequency of the resonator, in the number and type of side gates, in the in- and output capacitances, and whether there is a gap to put a transmon qubit in or not. Tab. 7.1 shows a list of the different designs.

The resonators are made by reactive ion etching of a sputtered niobium thinfilm on a sapphire substrate structured by optical lithography. Niobium has the advantage that it has a critical temperature where it gets superconducting of $T_c = 9.2$ K which is above the temperature of liquid helium $T = 4.2$ K. Therefore, to characterize the microwave properties of the resonators with different side gate configurations, and to learn about the cross coupling from the gate lines to the resonator, the resonators can be measured with a dipstick in a liquid helium dewar. All measurements were done with a *Rhode & Schwarz* ZVK vector network analyzer. The network analyzer was calibrated with the coaxial lines from its ports to the dipstick, but not with the wires inside the dipstick. To remove the effects of these wires from the measured data, a measurement of a niobium through was subtracted from all the further measurments. The open ports were terminated with a 50 Ω load to avoid signal reflection at the end which could cause unwanted interference.

7.2 Resonator with 3 hockey-stick flux lines

Fig. 7.1 shows the design of the first measured resonator, labeled "R1". It was designed for a fundamental frequency of $\nu_0 = 3.5$ GHz and a quality factor of $Q = 1600$ at the first harmonic frequency at which the resonator is intended to be operated.

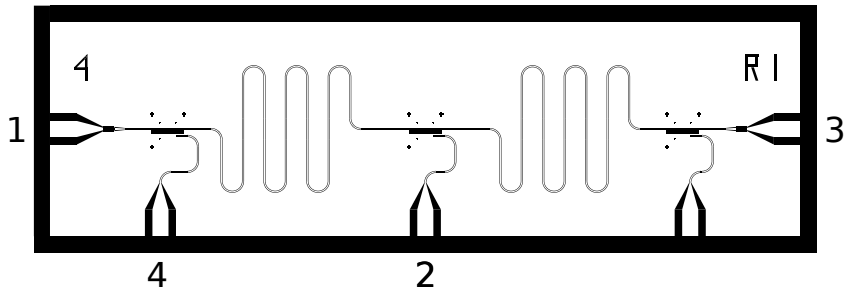

Figure 7.1: Designs of the resonators R1 with 3 hockey stick type flux lines. The numbers indicate with which port of the dipstick the corresponding port was connected.

7.2.1 Resonator characterization

At first the resonator, i. e. the insertion loss between port 1 and 3, was measured. The result of these measurement for a frequency range between 100 MHz and 20 GHz is shown in Fig. 7.2. The green line is the data where the sample is dipped comletely into the liquid helium and the red line is the data where the sample is still in the dewar but outside the liquid helium and is warmed up to a temperature slightly above the critical temperature where niobium get superconducting. The purpose of the latter measurement is to check which peaks have nothing to do with the superconductivity (and therefore with the resonator itself) and arise probably due to some resonances of the sample holder.

The data shows the first 6 resonances. The insertion loss of the resonances looks high due to the limited resolution. The real insertion loss at the resonances is lower as can be seen from separate measurements (see below). The background transmission measured above the critical temperature of niobium is less than -60 dB up to 9 GHz. At 9 GHz, there are some resanances probably from the sampleholder which are also visible in the transmission spectrum at 4.2 K. Up to 20 GHz, the background transmission is less than -40 dB.

Fig. 7.3 shows the transmission resonances at the fundamental and first harmonic frequency. The data which is obtained from the fitted Lorentzians is summed up in Tab. 7.2. The measured quality factors ($Q_{\mathrm{meas}} = 992$) are lower than the expected external quality factors ($Q_{\mathrm{ext}} = 1600$). This is probably due to the non vanishing internal quality factor (see subsection 2.3.2) at 4.2 K.

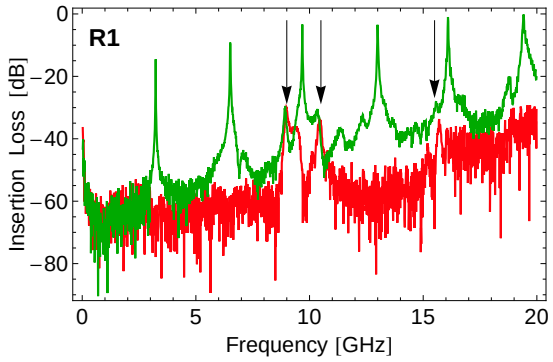

Figure 7.2: Measurement of the insertion loss between ports 1 and 3 for the resonator R1. The green line represents the data at a temperature of $T = 4.2$ K, the red line is a measurement at a temperature higher than the critical temperature of niobium $T_c = 9.2$ K. The arrows mark peaks which probably arise due to parts of the sample holder and are not features of the resonator.

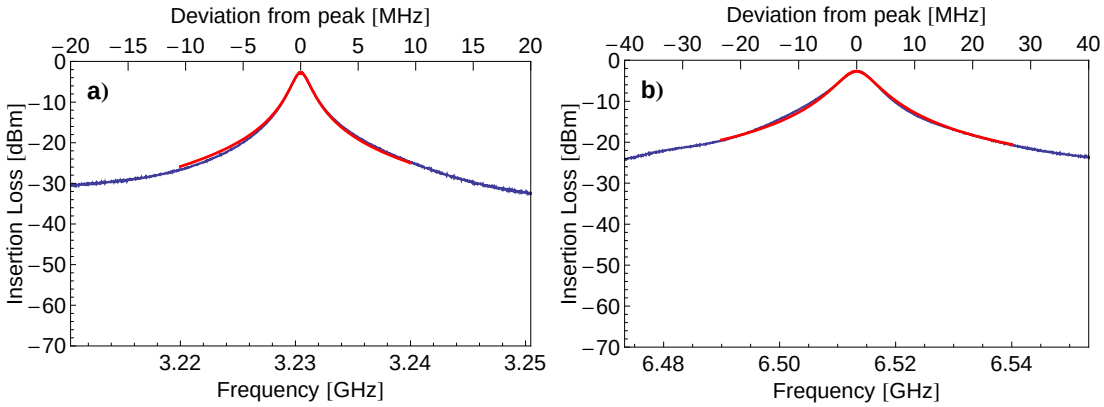

Figure 7.3: Data of the measurement between ports 1 and 3 of the resonator R1. Peaks at the fundamental (a) and first harmonic (b) frequency. Blue lines are data, red lines are Lorentzian fits.

	Fundamental	First harmonic
Frequency [GHz]	3.2305	6.5133
Quality factor	2086	992
Peak ins. loss [dBm]	-2.7	-2.7

Table 7.2: Data obtained from the Lorentzian fits to the measurements between port 1 and 3 of the resonator R1.

7.2.2 Cross coupling

To measure the cross coupling between the resonator and the flux lines, the insertion loss between port 1 and port 2 and 4 was measured. The results of these measurements for a frequency range between 100 MHz and 20 GHz are shown in Fig. 7.4. The detailed data of the peaks of the fundamental and first harmonic frequency are shown in Figs. 7.5 and 7.6 and Tabs. 7.3 and 7.4. One can see that there are peaks with the same quality factors as the resonator at the fundamental and the first harmonic frequency. Additionally there is a second peak about 100 MHz below the first harmonic frequency as shown in Figs. 7.7.

Above 10 GHz there are a lot of extra peaks which are not harmonics. This is probably not affecting the qubit, due its transition frequency at which it is operated is intended to be in the range between $4 - 7$ GHz.

At the first harmonic frequency one can observe a relatively strong cross coupling of -16.0 dB bewteen the resonator (port 1) and the flux line in the center of the chip (port 2). This could affect the measurement which is performed with microwaves at the resonator frequency. The coupling between the resonator and the flux line which is closer to the end of the resonator (port 4) is clearly weaker than the coupling to the center flux line. This could be understood if one considers that the standing wave in the cavity has its voltage antinodes at the boundaries and in the middle. While the line of port 2 lies very close to the middle, the line of port 4 is about 600 μm away from the voltage antinode at the beginning of the resonator.

The extra peak near the first harmonic frequency has an insertion loss of -28.9 dB, this might also affect the qubit if it is operated near resonant. Its origin is unknown and needs to be investigated, e. g. with more measurements on similar samples.

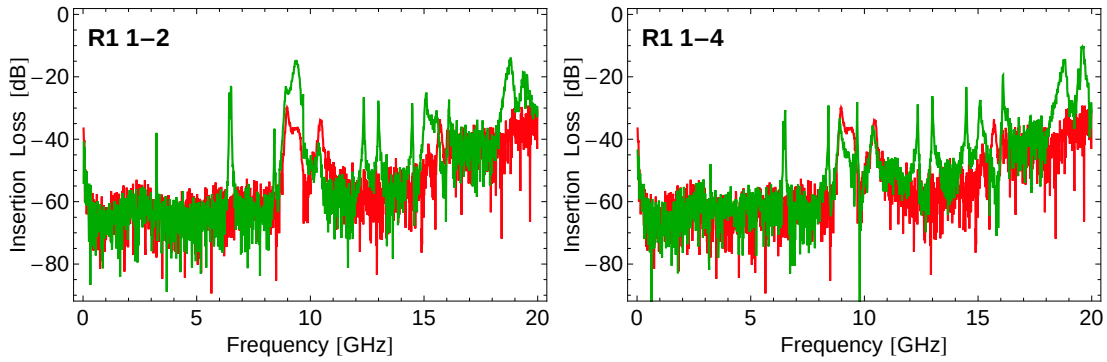

Figure 7.4: Measurements of the cross coupling between ports 1 and 2 (left) and ports 1 and 4 (right) for the resonator R1. The green line represents the data at a temperature of $T = 4.2$ K. The red line is the measurement of the bare resonator at a temperature higher than the critical temperature of niobium $T_c = 9.2$ K.

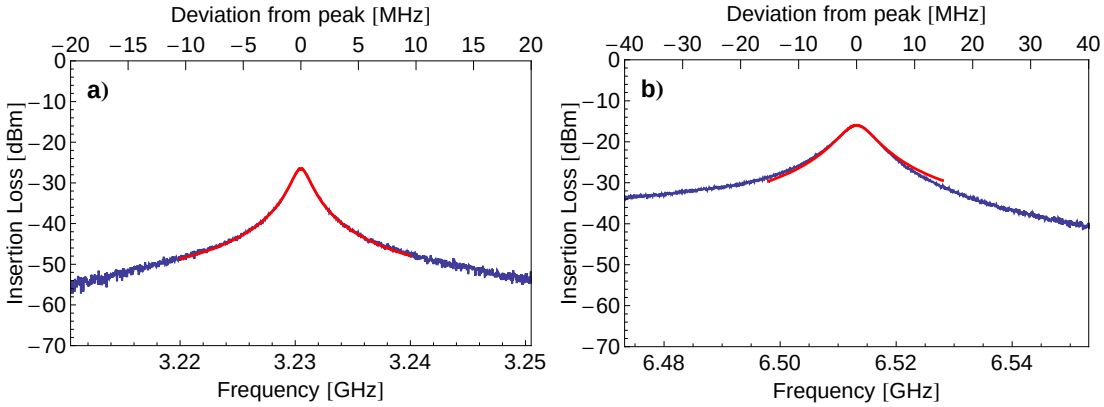

Figure 7.5: Data of the measurement between port 1 and center port 2 of resonator R1. Peak at the fundamental (a) and first harmonic (b) frequency. Blue line is data, red line is a Lorentzian fit.

	Fundamental	First harmonic
Frequency [GHz]	3.2305	6.5132
Quality factor	2099	1065
Peak ins. loss [dBm]	-26.5	-16.0

Table 7.3: Data obtained from the Lorentzian fit to the measurement between port 1 and center port 2 of the resonator R1.

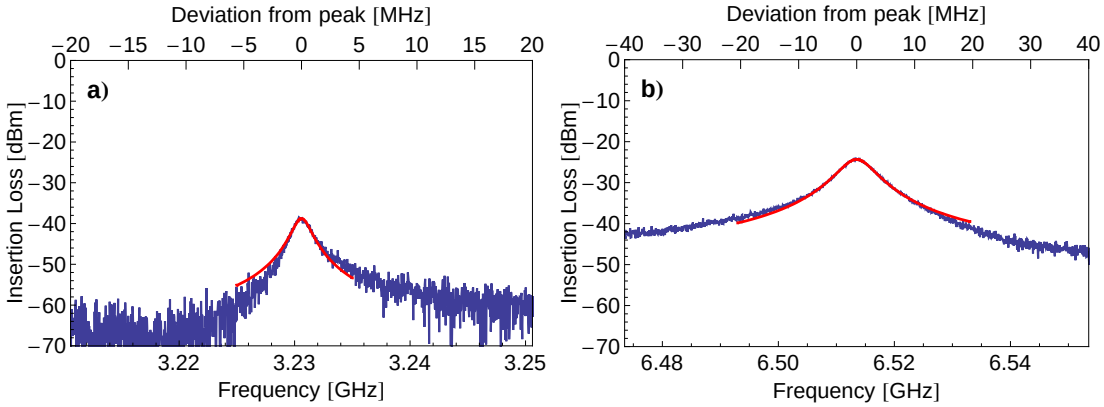

Figure 7.6: Data of the measurement between ports 1 and 4 of the resonator R1. Peak at the fundamental (a) and first harmonic (b) frequency. Blue line is data, red line is a Lorentzian fit.

	Fundamental	First harmonic
Frequency [GHz]	3.2306	6.5135
Quality factor	2019	1042
Peak ins. loss [dBm]	-38.7	-24.3

Table 7.4: Data obtained from the Lorentzian fits to the measurements between port 1 and 4 of the resonator R1.

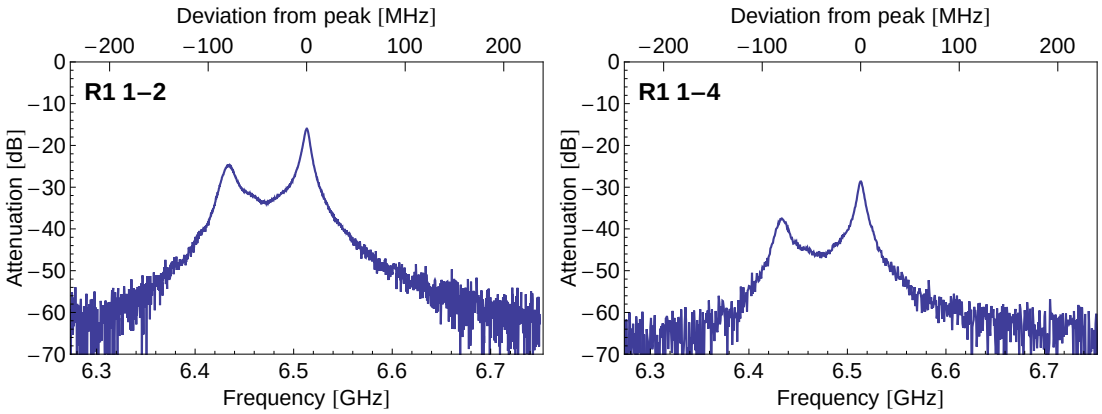

Figure 7.7: Double peak near the first harmonic frequency, which appears while measuring cross coupling from port 1 to 2 (left) and port 1 to 4 (right) of resonator R1.

7.3 Resonator with 3 short flux lines

The resonator "S1" shown in Fig. 7.8, is identical to the one discussed in the previous section aport from the type of flux lines.

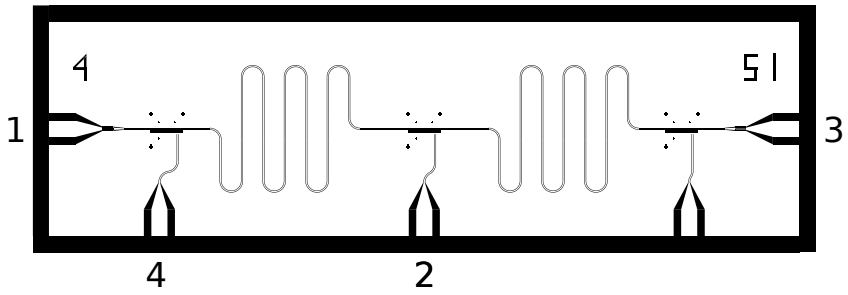

Figure 7.8: Designs of the resonators S1 with 3 short flux lines. The numbers indicate with which port of the dipstick the corresponding port was connected.

7.3.1 Resonator characterization

The result of the measurement between port 1 and 3 for a frequency range between 100 MHz and 20 GHz is shown in Fig. 7.9. The data looks very similar to the one of the

resonator R1, again the first six harmonics and some minor peaks due to sample holder resonances can be observed.

Fig. 7.10 shows the peaks at the fundamental and first harmonic frequency. The data which is obtained from the fitted Lorentzians is summed up in Tab. 7.5. All the data are very similar to the one of Resonator R1.

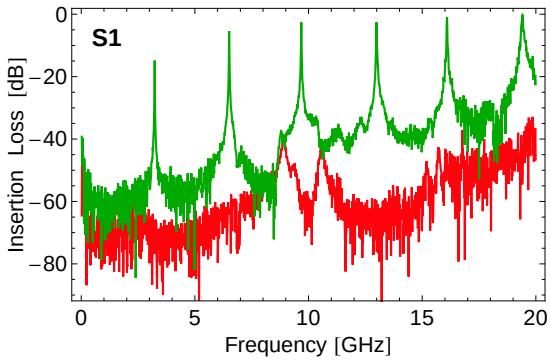

Figure 7.9: Measurement of the insertion loss between ports 1 and 3 for the resonator S1. The green line represents the data at a temperature of $T = 4.2$ K, the red line is a measurement at a temperature higher than the critical temperature of niobium $T_c = 9.2$ K.

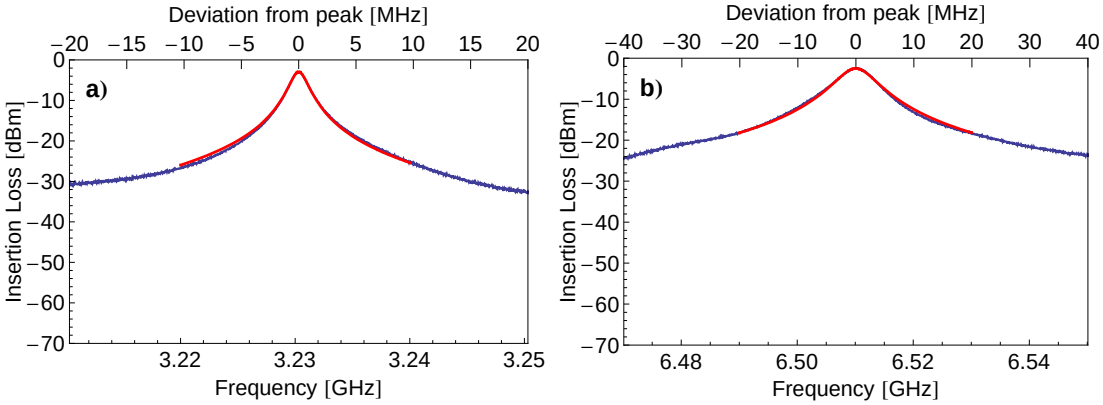

Figure 7.10: Data of the measurement between ports 1 and 3 of the resonator S1. Peaks at the fundamental (a) and first harmonic (b) frequency. Blue lines are data, red lines are Lorentzian fits.

	Fundamental	First harmonic
Frequency [GHz]	3.2303	6.5101
Quality factor	2091	970
Peak ins. loss [dBm]	-3.0	-2.5

Table 7.5: Data obtained from the Lorentzian fits to the measurements between port 1 and 3 of the resonator S1.

7.3.2 Cross coupling

The results of the cross coupling measurements for a frequency range between 100 MHz and 20 GHz are shown in Fig. 7.11. The detailed data of the peaks of the fundamental and first harmonic frequency are shown in Figs. 7.12 and 7.13 and Tabs. 7.6 and 7.7.

It is outstanding, that the coupling between the resonator and the sidegates is weaker than in resonator R1. At the fundamental frequency, the cross coupling to the center gate is even 10 dB weaker at the fundamental frequency. The general smaller cross coupling makes sense, because the geometry of the short lines suggests a smaller capacitance to the resonator than the one of the hockey stick lines.

As in the resonator R1, there is a second peak about 100 MHz below the first harmonic frequency as shown in Figs. 7.14.

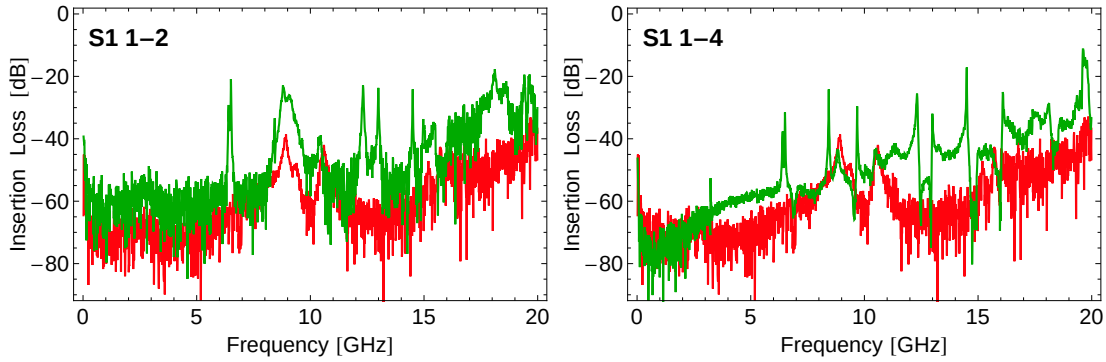

Figure 7.11: Measurements of the cross coupling between ports 1 and 2 (left) and ports 1 and 4 (right) for the resonator S1. The green line represents the data at a temperature of $T = 4.2$ K. The red line is the measurement of the bare resonator at a temperature higher than the critical temperature of niobium $T_c = 9.2$ K.

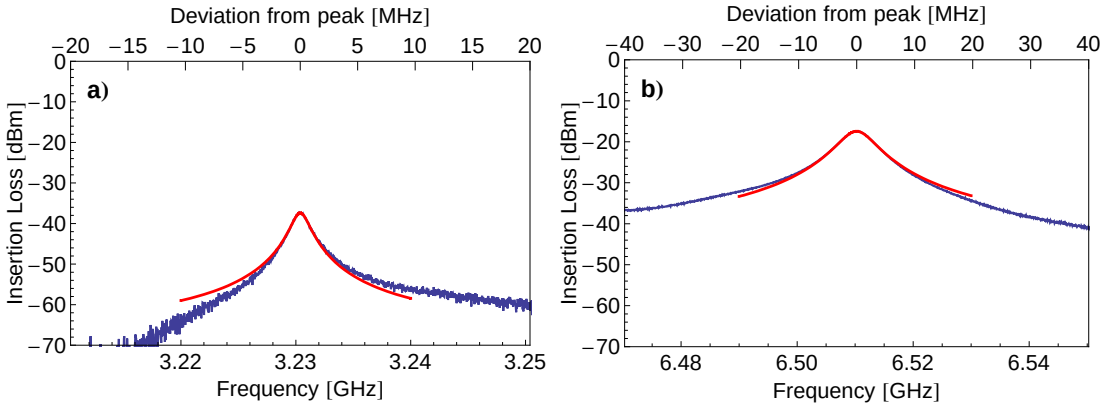

Figure 7.12: Data of the measurement between port 1 and center port 2 of the resonator S1. Peak at the fundamental (a) and first harmonic (b) frequency. Blue line is data, red line is a Lorentzian fit.

	Fundamental	First harmonic
Frequency [GHz]	3.2304	6.5103
Quality factor	2106	1040
Peak ins. loss [dBm]	-37.4	-17.4

Table 7.6: Data obtained from the Lorentzian fit to the measurement between port 1 and center port 2 of the resonator S1.

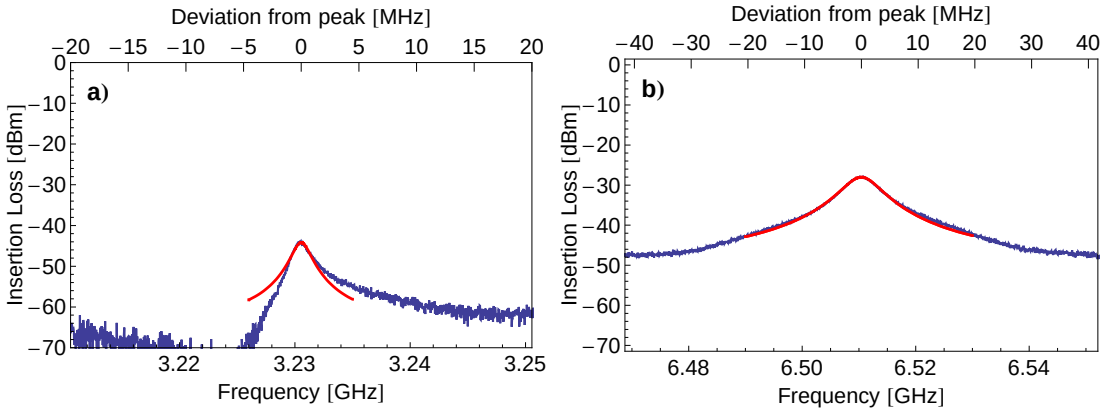

Figure 7.13: Data of the measurement between ports 1 and 4 of the resonator S1. Peak at the fundamental (a) and first harmonic (b) frequency. Blue line is data, red line is a Lorentzian fit.

	Fundamental	First harmonic
Frequency [GHz]	3.2306	6.5104
Quality factor	2060	977
Peak ins. loss [dBm]	-44.2	-28.0

Table 7.7: Data obtained from the Lorentzian fits to the measurements between port 1 and 4 of the resonator S1.

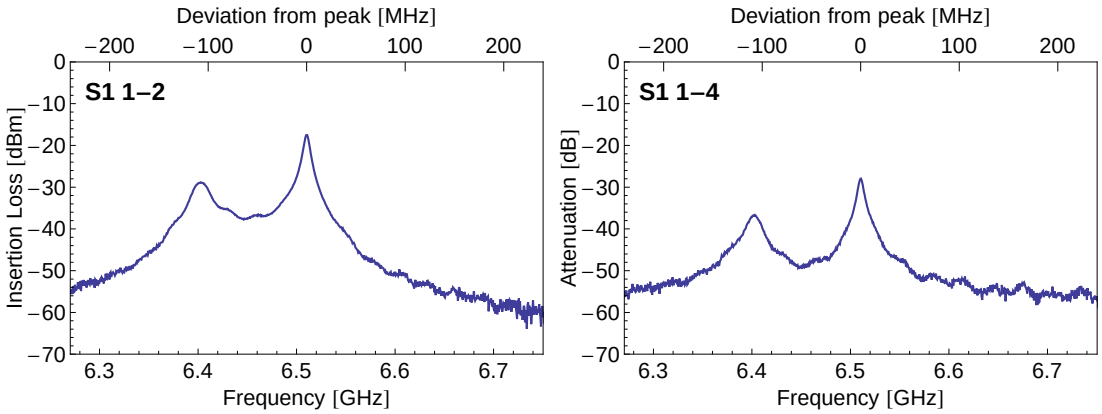

Figure 7.14: Double peak near the first harmonic frequency, which appears while measuring cross coupling from port 1 to 2 (left) and port 1 to 4 (right) of resonator S1.

7.4 Resonator with 2 short flux lines

The resonator "J1" shown in Fig. 7.15, is designed for a fundamental frequency of 7 GHz with a quality factor of $Q = 7600$. It has two short flux lines near the beginning and the end of the resonator.

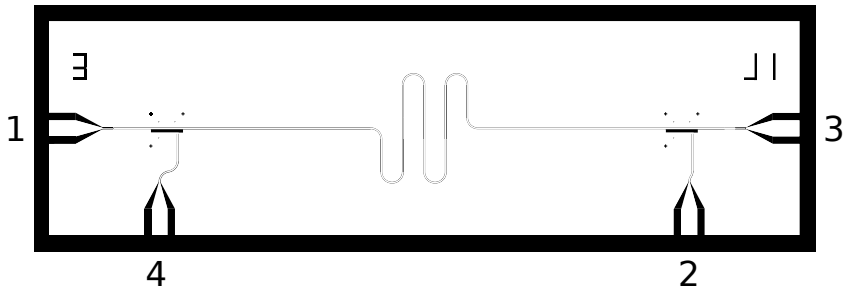

Figure 7.15: Designs of the resonators J1 with 2 short flux lines. The numbers indicate with which port of the dipstick the corresponding port was connected.

7.4.1 Resonator characterization

The result of the measurement between port 1 and 3 for a frequency range between 100 MHz and 20 GHz is shown in Fig. 7.16.

The data shows the first three resonances and a resonance from the sample holder between 9 and 10 GHz.

Fig. 7.17 shows the peaks at the fundamental and first harmonic frequency. The data which is obtained from the fitted Lorentzians is summed up in Tab. 7.8.

The insertion loss at these resonances is clearly higher than in the previously measured resonators. Also the quality factors are much smaller than the expected external quality factor. Again the limiting factor could be the internal quality factor which is not vanishing at 4.2 K.

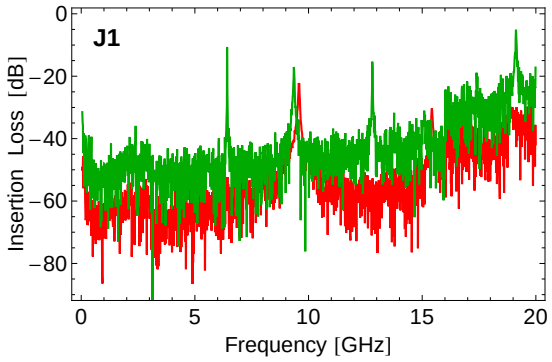

Figure 7.16: Measurement of the insertion loss between ports 1 and 3 for the resonator J1. The green line represents the data at a temperature of $T = 4.2$ K, the red line is a measurement at a temperature higher than the critical temperature of niobium $T_c = 9.2$ K.

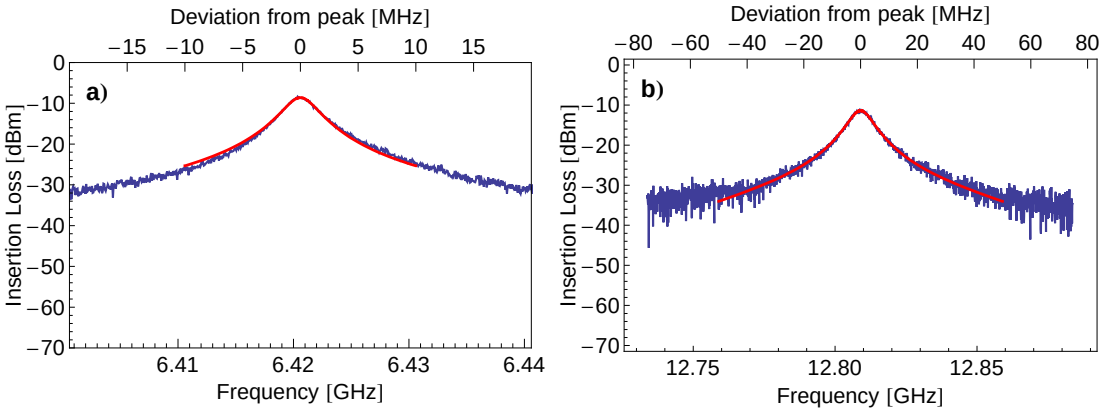

Figure 7.17: Data of the measurement between ports 1 and 3 of the resonator J1. Peaks at the fundamental (a) and first harmonic (b) frequency. Blue lines are data, red lines are Lorentzian fits.

	Fundamental	First harmonic
Frequency [GHz]	6.4206	12.8091
Quality factor	2168	1438
Peak ins. loss [dBm]	-8.6	-11.4

Table 7.8: Data obtained from the Lorentzian fits to the measurements between port 1 and 3 of the resonator J1.

7.4.2 Cross coupling

The results of the cross coupling measurements for a frequency range between 100 MHz and 20 GHz are shown in Fig. 7.18. The detailed data of the peaks of the fundamental and first harmonic frequency are shown in Figs. 7.19 and 7.20 and Tabs. 7.9 and 7.10.

The cross coupling is considerably weaker than in the measured resonators with three gate lines. Below 10 GHz only the sample holder resonance has a lower insertion loss than −30 dB. The coupling between port 1 and 4 is stronger than between port 1 and 2, although they are both near the boundary of the cavity. But port 1 is much nearer to port 4 than to port 2. This could indicate that the coupling arises not only due to coupling between the resonator and the gatelines, but also due to the coupling of the launchers of the ports.

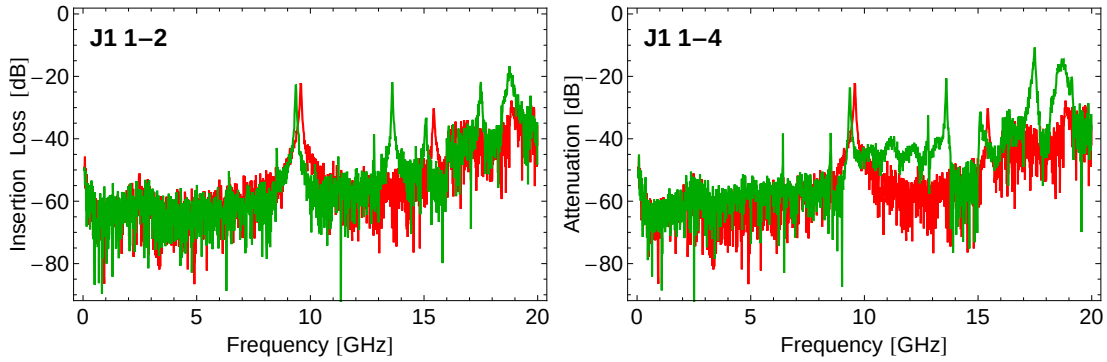

Figure 7.18: Measurements of the cross coupling between ports 1 and 2 (left) and ports 1 and 4 (right) for the resonator J1. The green line represents the data at a temperature of $T = 4.2$ K. The red line is the measurement of the bare resonator at a temperature higher than the critical temperature of niobium $T_c = 9.2$ K.

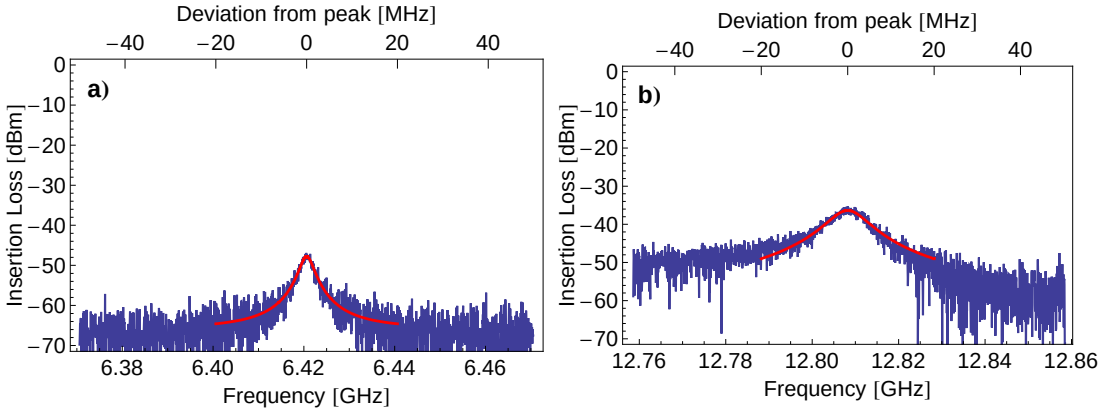

Figure 7.19: Data of the measurement between port 1 and center port 2 of the resonator J1. Peak at the fundamental (a) and first harmonic (b) frequency. Blue line is data, red line is a Lorentzian fit.

	Fundamental	First harmonic
Frequency [GHz]	6.4206	12.8082
Quality factor	2115	1415
Peak ins. loss [dBm]	-47.8	-36.4

Table 7.9: Data obtained from the Lorentzian fit to the measurement between port 1 and center port 2 of the resonator J1.

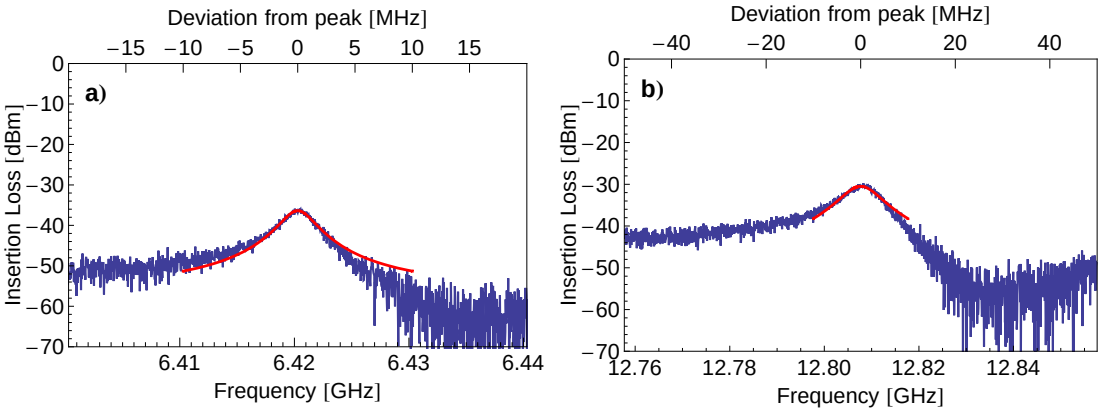

Figure 7.20: Data of the measurement between ports 1 and 4 of the resonator J1. Peak at the fundamental (a) and first harmonic (b) frequency. Blue line is data, red line is a Lorentzian fit.

	Fundamental	First harmonic
Frequency [GHz]	6.4203	12.8077
Quality factor	2207	1468
Peak ins. loss [dBm]	-36.4	-30.5

Table 7.10: Data obtained from the Lorentzian fits to the measurements between port 1 and 4 of the resonator J1.

7.5 Resonator with 2 charge/drive lines

The resonator "E5" shown in Fig. 7.21, is designed for a fundamental frequency of 7 GHz with a quality factor of $Q = 1900$. It has two charge/drive lines near the beginning and the end of the resonator.

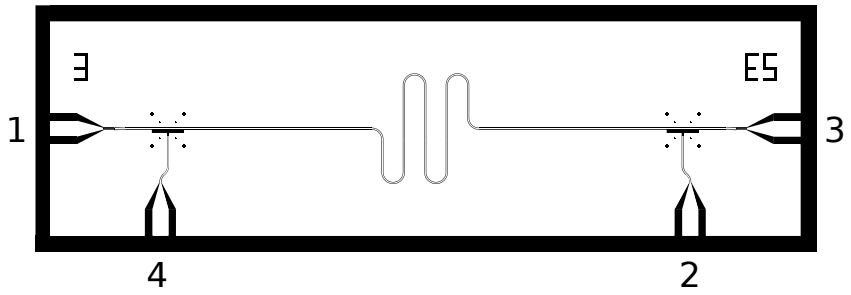

Figure 7.21: Designs of the resonators E5 with 2 charge/drive lines. The numbers indicate with which port of the dipstick the corresponding port was connected.

7.5.1 Resonator characterization

The result of the measurement between port 1 and 3 for a frequency range between 100 MHz and 20 GHz is shown in Fig. 7.22.

The data shows the first three resonances and a resonance from the sample holder between 9 and 10 GHz, as in the 7 GHz resonator J1.

Fig. 7.23 shows the peaks at the fundamental and first harmonic frequency. The data which is obtained from the fitted Lorentzians is summed up in Tab. 7.11.

The insertion loss at these resonances is the same as in the resonators R1 and S1 which have a similar external quality factor.

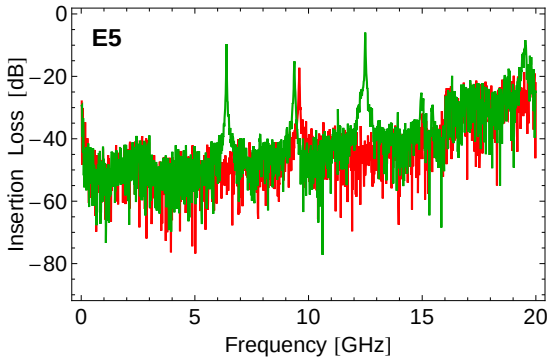

Figure 7.22: Measurement of the insertion loss between ports 1 and 3 for the resonator E5. The green line represents the data at a temperature of $T = 4.2$ K, the red line is a measurement at a temperature higher than the critical temperature of niobium $T_c = 9.2$ K.

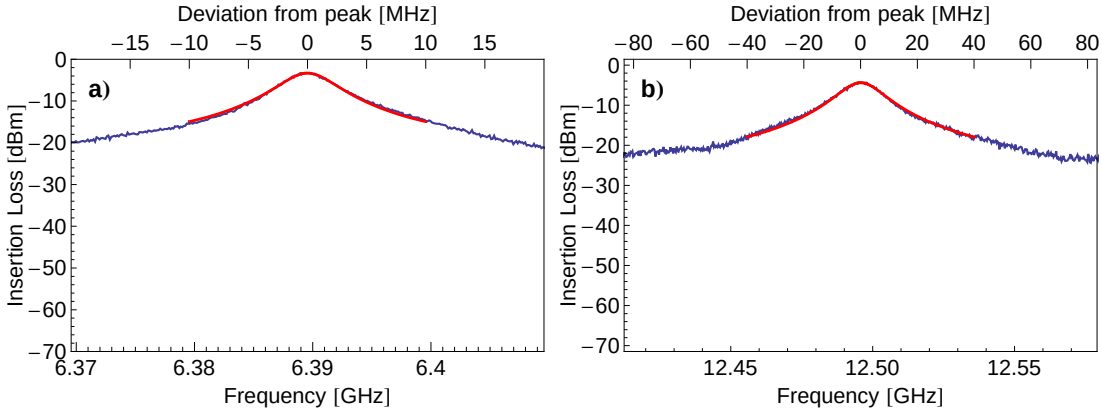

Figure 7.23: Data of the measurement between ports 1 and 3 of the resonator E5. Peaks at the fundamental (a) and first harmonic (b) frequency. Blue lines are data, red lines are Lorentzian fits.

	Fundamental	First harmonic
Frequency [GHz]	6.3896	12.4957
Quality factor	1321	770
Peak ins. loss [dBm]	-3.3	-4.4

Table 7.11: Data obtained from the Lorentzian fits to the measurements between port 1 and 3 of the resonator E5.

7.5.2 Cross coupling

The results of the cross coupling measurements for a frequency range between 100 MHz and 20 GHz are shown in Fig. 7.24. The detailed data of the peaks of the fundamental and first harmonic frequency are shown in Figs. 7.25 and 7.26 and Tabs. 7.12 and 7.13.

The cross coupling is higher than in the resonator J1. This was expected, because the capacitance of the charge gate line to the resonator is higher than the capacitance of the shorted gate lines to the resonator.

Furthermore, one can observe that resonance at the first harmonic is not exactly twice the fundamental frequency but lower, and that the quality factor of this resonance is similar to that of the fundamental frequency, although it should be about half of it.

As in the cross coupling of the resonators R1 and S1, a second peak near the first harmonic frequency can be observed as shown in Fig. 7.27. The peak is around 150 MHz below the first harmonic, and has a similar insertion loss as the resonance at the first harmonic when it is measured between port 1 and port 2. The measurement between port 1 and port 4 (which is nearer to the input than port 2) shows a higher loss at the extra peak. It is not clear whether this extra peak has the same origin as the ones in the resonators R1 and S1. Again, more samples have to be measured to investigate this phenomena.

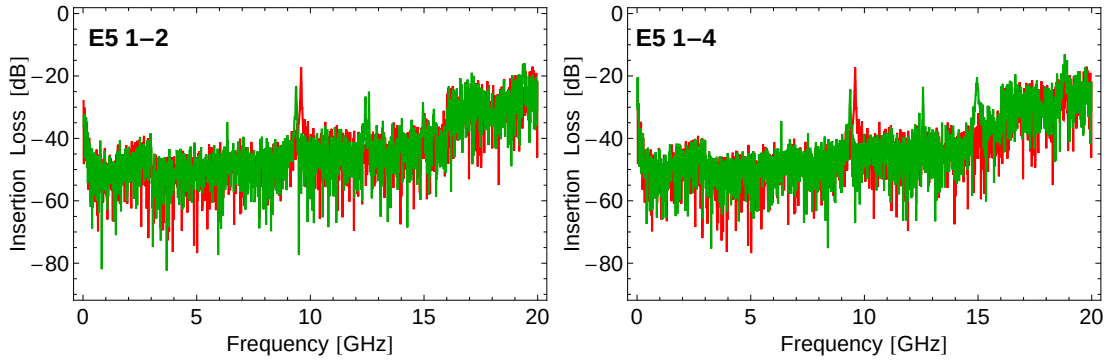

Figure 7.24: Measurements of the cross coupling between ports 1 and 2 (left) and ports 1 and 4 (right) for the resonator E5. The green line represents the data at a temperature of $T = 4.2$ K. The red line is the measurement of the bare resonator at a temperature higher than the critical temperature of niobium $T_c = 9.2$ K.

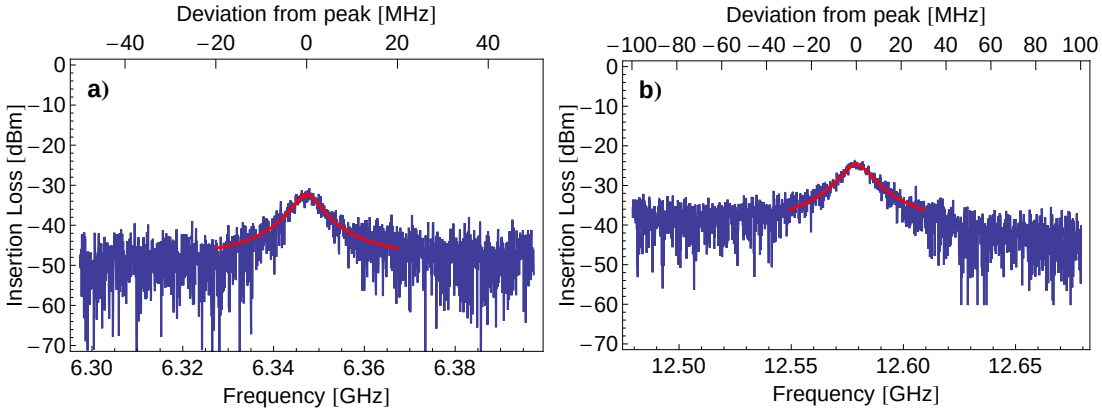

Figure 7.25: Data of the measurement between port 1 and center port 2 of the resonator E5. Peak at the fundamental (a) and first harmonic (b) frequency. Blue line is data, red line is a Lorentzian fit.

	Fundamental	First harmonic
Frequency [GHz]	6.3473	12.5790
Quality factor	1049	926
Peak ins. loss [dBm]	-32.4	-24.7

Table 7.12: Data obtained from the Lorentzian fit to the measurement between port 1 and center port 2 of the resonator E5.

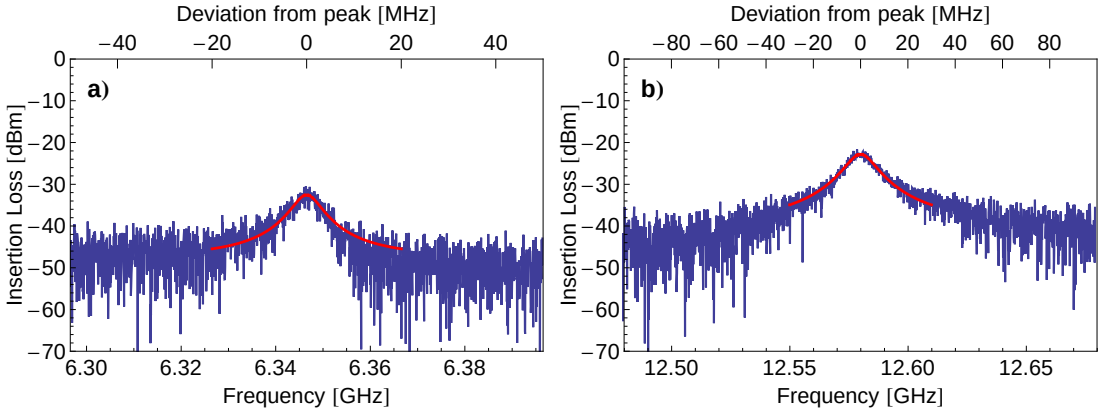

Figure 7.26: Data of the measurement between ports 1 and 4 of the resonator E5. Peak at the fundamental (a) and first harmonic (b) frequency. Blue line is data, red line is a Lorentzian fit.

	Fundamental	First harmonic
Frequency [GHz]	6.3465	12.5799
Quality factor	1082	981
Peak ins. loss [dBm]	-32.5	-22.8

Table 7.13: Data obtained from the Lorentzian fits to the measurements between port 1 and 4 of the resonator E5.

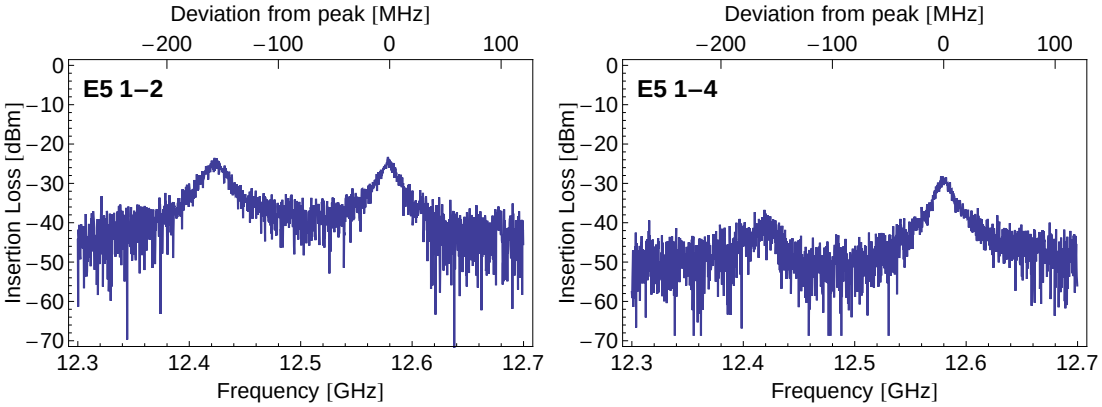

Figure 7.27: Double peak near the first harmonic frequency, which appears while measuring cross coupling from port 1 to 2 (left) and port 1 to 4 (right) of resonator E5.

7.6 Resonator with the 2-port flux lines

Fig. 7.28 shows the design of the resonator "K5" with the 2-port flux lines. It was designed for a fundamental frequency of $\nu_0 = 3.5$ GHz and a quality factor of $Q = 1600$ at the first harmonic frequency at which the resonator is intended to be operated.

The result of the measurement between port 1 and 3 for a frequency range between 100 MHz and 20 GHz is shown in Fig. 7.29. One can observe the six first resonances and resonance of the sampleholder at 8 GHz.

The results of the cross coupling measurements for a frequency range between 100 MHz and 20 GHz are shown in Fig. 7.30. One can identify the first 5 harmonics and some additional peaks above 10 GHz as well as the sample holder resonance at 8 GHz and an additional peak at 5 GHz. But this peak is below -40 dB and therefore won't affect the qubit much.

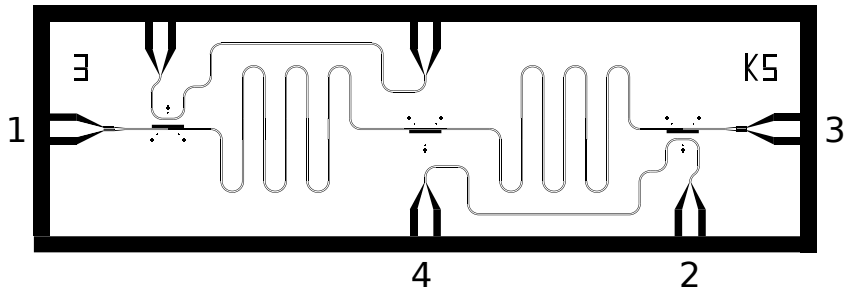

Figure 7.28: Designs of the resonators K5 with two 2-port flux lines. The numbers indicate with which port of the dipstick the corresponding port was connected.

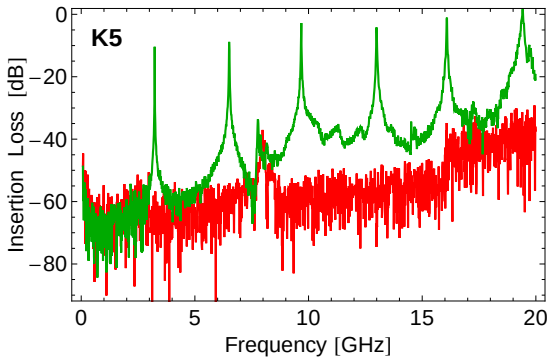

Figure 7.29: Measurement of the insertion loss between ports 1 and 3 for the resonator K5. The green line represents the data at a temperature of $T = 4.2$ K, the red line is a measurement at a temperature higher than the critical temperature of niobium $T_c = 9.2$ K.

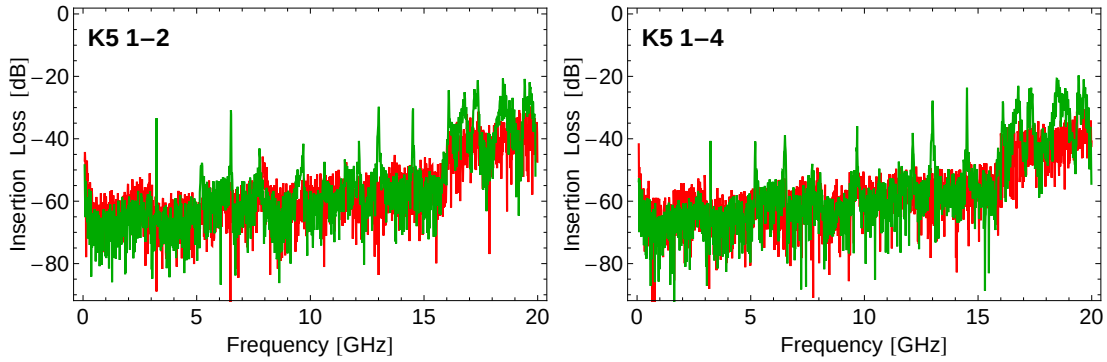

Figure 7.30: Measurements of the cross coupling between ports 1 and 2 (left) and ports 1 and 4 (right) for the resonator K5. The green line represents the data at a temperature of $T = 4.2$ K. The red line is the measurement of the bare resonator at a temperature higher than the critical temperature of niobium $T_c = 9.2$ K.

7.7 Resonator with charge and short flux line combined

Fig. 7.31 shows the design of the resonator "M1" with the charge and short flux line combined. It was designed for a fundamental frequency of $\nu_0 = 3.5$ GHz and a quality factor of $Q = 3800$ at the first harmonic frequency at which the resonator is intended to be operated.

The result of the measurement between port 1 and 3 for a frequency range between 100 MHz and 20 GHz is shown in Fig. 7.32. Apart from the first six resonances and a sampleholder resonance at 8 GHz, one can observe peaks with low insertion losses at 5 GHz and 11 GHz.

These peaks can also be found in the cross coupling as shown in Fig. 7.33. The resonance at 5 GHz is not present in the coupling between the resonator and the flux line, but in the coupling between the resonator and the charge line, this resonance has an insertion loss of only −14.3 dB, which indicates a very strong coupling.

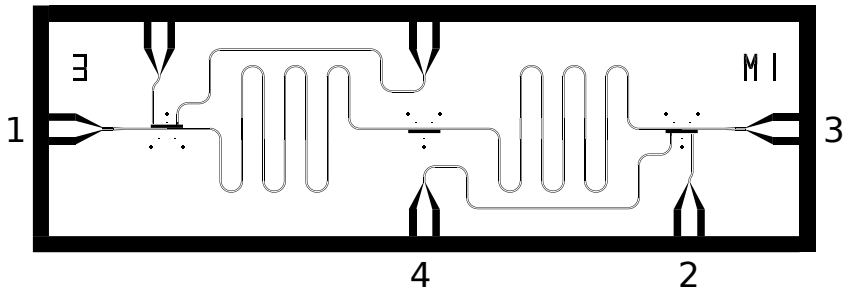

Figure 7.31: Designs of the resonators M1 with two 2-port flux lines. The numbers indicate with which port of the dipstick the corresponding port was connected.

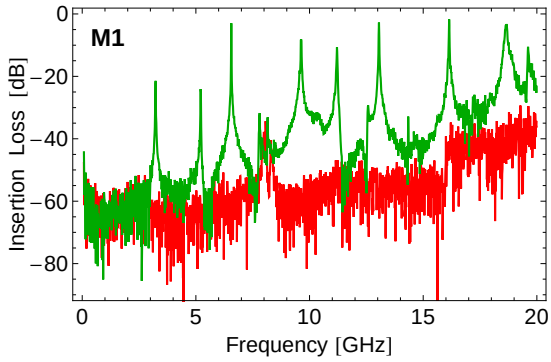

Figure 7.32: Measurement of the insertion loss between ports 1 and 3 for the resonator M1. The green line represents the data at a temperature of $T = 4.2$ K, the red line is a measurement at a temperature higher than the critical temperature of niobium $T_c = 9.2$ K.

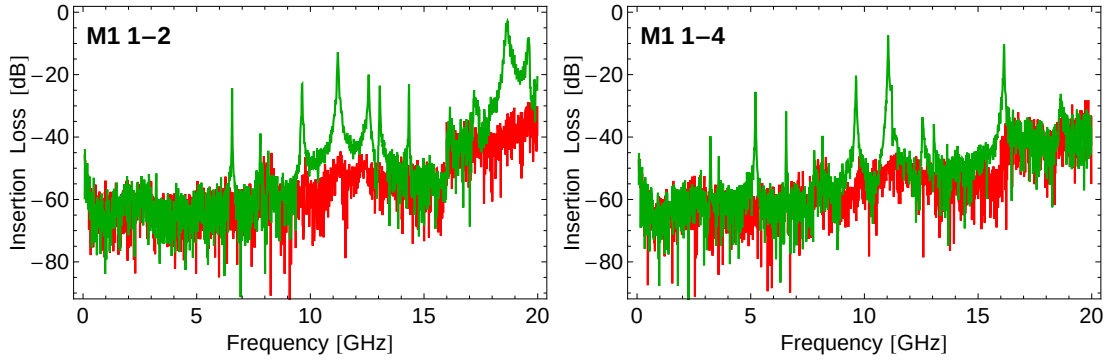

Figure 7.33: Measurements of the cross coupling between ports 1 and 2 (left, resonator–flux line) and ports 1 and 4 (right, resonator–charge line) for the resonator M1. The green line represents the data at a temperature of $T = 4.2$ K. The red line is the measurement of the bare resonator at a temperature higher than the critical temperature of niobium $T_c = 9.2$ K.

7.8 Final considerations

The measurements of the 3.5 GHz resonators show that they have a relatively high coupling between the resonator and the flux side gate at the first harmonic frequency where the resonator is intended to be operated. Also both resonators show an extra peak around 100 MHz below the first harmonic frequency. This can also influence the measurements or the qubits when they are operated near resonanc.

Better results can be observed with the 7 GHz resonators. All the cross couplings

show insertion losses at the fundamental frequency below -30 dB.

A side gate divides the ground plane in two parts which are on the chip only connected through a thin section (or not at all in the case of the charge lines). Although they are all bonded to the ground of the sample holder, some local voltage differences can occur. This "dividing" of the ground plane could be one reason that the resonators with just two side gates show better results than the ones with three side gates. A possible improvement could be achieved, if the ground planes are better connected to each other. This could be done with bondings between the neighbouring ground planes.

The resonator with the 2-port flux line shows a nice resonator characteristic and a low cross coupling and is therefore a candidate to be used to put a qubit in.

The chip with the combined flux and charge gate shows many extra resonances with small insertion loss. Their origin is not known yet and one would have to perform more experiments on similar designs or to do simulations with good models to investigate it.

Freq. [GHz]	Q	Qubit type	Gates	# of copies
7	7600	CPB	2 charge gates	2
7	1900	CPB	2 charge gates	2
7	7600	Transmon	2 charge gates	4
7	1900	Transmon	2 charge gates	4
3.5	3800	Transmon	1 charge gate	4
3.5	1600	Transmon	1 charge gate	4
7	7600	CPB	2 HS flux gates	2
7	1900	CPB	2 HS flux gates	2
7	7600	CPB	2 short flux gates	2
7	1900	CPB	2 short flux gates	2
7	7600	Transmon	2 HS flux gates	4
7	1900	Transmon	2 HS flux gates	4
7	7600	Transmon	2 short flux gates	4
7	1900	Transmon	2 short flux gates	4
3.5	3800	Transmon	2 flux 2 terminals	4
3.5	1600	Transmon	2 flux 2 terminals	4
3.5	3800	Transmon	2 HS flux and charge gates	3
3.5	1600	Transmon	2 HS flux and charge gates	2
3.5	3800	Transmon	2 short flux and charge gates	4
3.5	1600	Transmon	2 short flux and charge gates	4
3.5	3800	Transmon	1 HS flux and charge gate	3
3.5	1600	Transmon	1 HS flux and charge gate	3
3.5	3800	Transmon	1 short flux and charge gate	4
3.5	1600	Transmon	1 short flux and charge gate	4
3.5	1600	Transmon	3 short flux gates	2
3.5	3800	Transmon	3 short flux gates	2
3.5	1600	Transmon	3 HS flux gates	2
3.5	3800	Transmon	3 HS flux gates	2

Table 7.1: List of different designs of the resonators with sidegates. Short flux gate denotes the design in Fig. 5.2 a), HS refers to the hockey stick design as in Fig. 5.2 b).

8 Conclusion

8.1 What has been done?

The main goal of this thesis was to design new side gates that will allow local qubit control in a circuit QED system. To design the new side gates *Mathematica*-functions have been written which can be combined in a modular way to generate the whole chips with resonators and side gates with only a few lines of code. To optimize the parameters of the design, a model and the corresponding formalism has been worked out. This model allows to calculate the effects of the additional side gates to the decay time of the qubit as well as the expected Rabi frequency. As input parameters, this model requires the capacitances between the gate line and the parts of the Cooper pair box. To simulate these capacitances, the convevtional CPB and the transmon have been simulated with Maxwell® 3D, a 3D finite elements software that simulates electromagnetic fields.

Based on these calculations, a charge gate line and three different types of flux gate lines have been designed. The charge gate line is just a line like the resonator which couples capacitively to the Cooper pair box. This line couples directly, without being filtered by the cavity, which allows to drive the qubit faster at a constant power than via the resonator. The distance between the charge line and the place where the qubit will be inserted is fixed. This means that the minimum capacitance between the line and the qubit is given, but by the design of the Cooper pair box, the capacitance can still be increased, which will increase the coupling strength but also the decay rate.

For the flux lines, three different designs were created: A two port flux line and two different lines that are shorted to ground on the chip. The two port flux line is a line with a current source and sink, that passes near the qubit. An applied current will induce a flux which allows to control the qubit transition frequency. The shorted lines have just one port for a current source, but no sink. This gives a much lower capacitive coupling to the qubit which results in a lower decay rate.

The new gate lines require additional wiring in the cryostat. For the charge gate lines, the requirements are similar as for the lines that couple to the resonator and can be used to measure or drive the qubit state. The flux lines need to carry current, rather than voltage. To prevent a heating of the lowest temperature stages in the cryostat due to the higher power dissipation, a new cabling was designed and new combined powder filters with copper wire and additional capacitances were fabricated.

The microwave properties of six of the 30 different resonators have been characterized

and the cross coupling from the resonator to the side gates has been measured. The measurements showed, that the cross coupling in the resonators with three side gates is higher than in the resonators with two side gates. This might be due to the fragmentation of the ground plane in parts that are only connected by very narrow lines. Also the measurement of the resonator with the flux and charge gates combined shows many resonances with low insertion loss. Befor they can be used with qubits, one has to investigate their origin and to adapt the design such that they won't occur anymore.

8.2 Next steps

As a next step, the different behaviour of the resonators with different numbers of side gates has to be understood. To achieve this, more measurements of resonators have to be done. Also one has to check the effect of small modifications to the resonator, e. g. bondings that connect the separated ground planes among each other.

The cabling for the new gate lines could be implemented and the the new bias tees K251 could be measured and compared to the simulations done in section 6.1.

If this is done, one could try to perform first experiments with qubits in the resonator. These experiments will show whether the calculated values such as the decay time and the control abilities are correct.

Some simulated parameters are believed to be unreliable. E. g. for the mutual inductance, one expects higher values than simulated, because the simulation software cannot handle superconducting materials which expel the magnetic flux and therefore might increase the range of the magnetic field near their surface. Also the capacitances between the resonator and the shorted flux lines, which were simulated with a simple model in Microwave Office®, are probably imprecise. It would be good to simulate these properties with software that is able to perform electrodynamic simulations and that can handle superconducting materials.

9 Acknowledgements

First of all, I would like to thank my supervisor Prof. Dr. Andreas Wallraff who gave me the opportunity to do my diploma thesis on this fascinating topic. I also want to thank him for all his explanations and inspiring advices. I also would like to thank all my collaborators in the group. With Dr. Peter Leek I had some fruitful discussions about the designs and the calculations. He showed me a lot of Mathematica tricks, introduced me into simulation and design softwares and fabricated the chips which I designed. Romeo Bianchetti taught me a lot about the experimental setup, about microwaves and how to use Maxwell 3D. Andreas Fragner always had time to answer my questions and together we developped the new combined powder filters and assembled a lot of them. Johannes Fink and Matthias Baur showed me how to perform measurements and how to handle the cryostat. Martin Göppl is working hard to put a qubit in one of the resonators I designed and I look forward to measure it. Thank you all, it was a pleasure working with you.

A Numerical calculation of the decay times

This appendix shows the *Mathematica* notebook that can be used to calculate the decay rates of a Cooper pair box due to capacitive coupling to charge noise or due to inductive coupling to flux noise. The function which calculates the eigenvectors of the Hamiltonian and orders it according to the eigenvalues is based on a *Mathematica* notebook by Alexandre Blais (cf. section 4.2).

Definitions and Calculations

```
Φ0 = 2.067833636 × 10^-15; hbar = 6.626068 × 10^-34 / (2 π);
kb = 1.3806503 10^-23; GHz = 10^9; e = 1.60217646 * 10^-19;
```

Number of the highest charge state which is taken into account:

```
dim = 5;
```

n is a matrix containing all the charge eigenstates, NN is the charge number operator:

```
n = IdentityMatrix[2 * dim + 1];
NN = DiagonalMatrix[Range[-dim, dim]];
```

Defining H_{el} and H_J:

```
Hel := 4 Ec (NN - IdentityMatrix[2 * dim + 1] ng)^2;
Hj :=
  - Ej Sum[Cos[π Φ / Φ0] / 2 (Transpose[{n[[i]]}].{n[[i + 1]]} + Transpose[{n[[i + 1]]}].{n[[i]]}) +
     i d Sin[π Φ / Φ0] / 2 (Transpose[{n[[i]]}].{n[[i + 1]]} - Transpose[{n[[i + 1]]}].{n[[i]]}), {i,
     1, 2 * dim}];
```

Function which calculates the eigenvectors of the Hamiltonian and orders it according to the eigenvalues:

```
eigvecs[params__] :=
 Module[{temp, new, evals, evecs},
  {evals, evecs} = Eigensystem[Hel + Hj /. params];
  temp = Table[{evals[[i]], evecs[[i]]}, {i, 1, 2 * dim + 1}];
  new = Chop[Sort[temp, (#1[[1]] < #2[[1]]) &]];
  Transpose[Flatten[Drop[Transpose[new], 1], 1]]
 ]
```

Noise spectral density functions:

$$\text{Sn}[\omega\_, \text{T}\_] := \frac{2\,\text{hbar}\,\omega\,\text{R}}{1 - \text{Exp}\left[\frac{-\text{hbar}\,\omega}{\text{kb T}}\right]} \left(\beta \frac{\text{C}\Sigma}{2\,\text{e}}\right)^2;$$

$$\text{S}\phi[\omega\_, \text{T}\_] := \text{M}^2 \frac{2\,\text{hbar}\,\omega}{\text{R}\left(1 - \text{Exp}\left[\frac{-\text{hbar}\,\omega}{\text{kb T}}\right]\right)};$$

Function which calculates T_1 due to charge noise:

```
T1charge[params__] := Module[{StateMatrix, A, A2},
  StateMatrix = eigvecs[params];
  A = - 4 Ec 2 (NN - IdentityMatrix[2 * dim + 1] ng) /. params;
  A2 = Norm[(ConjugateTranspose[StateMatrix][[2]].
        A.Transpose[{Transpose[StateMatrix][[1]]}])]^2 /. params;
  1 / (A2 1 / hbar^2 Sn[ω, T]) /. params
 ]
```

Function which calculates T_1 due to flux noise:

```
T1flux[params__] := Module[{StateMatrix, A, A2},
  StateMatrix = eigvecs[params];
  A = Ej π/Φ0
      Sum[Sin[π Φ/Φ0]/2 (Transpose[{n[[i]]}].{n[[i + 1]]} + Transpose[{n[[i + 1]]}].{n[[i]]}) -
        d i Cos[π Φ/Φ0]/2 (Transpose[{n[[i]]}].{n[[i + 1]]} - Transpose[{n[[i + 1]]}].{n[[i]]}),
      {i, 1, 2 * dim}] /. params;
  A2 = Norm[(ConjugateTranspose[StateMatrix][[2]].A.
        Transpose[{Transpose[StateMatrix][[1]]}])]^2 /. params;
  1 / (A2 1/hbar^2 Sϕ[ω, T]) /. params
]
```

Plots

Defining some parameters which are reasonnable for a Cooper pair box:

```
params = {C1 → 0.0016 * 10^-15, C2 → 0.046 10^-15, C3 → 0.41 10^-15, C4 → 3.63 10^-15, Cj → 4. 10^-15,
   R → 50., Ej → 3.7 GHz 2 π hbar, ng → 0.5, ω → 5.4 GHz 2 π, Ec → 4.43 GHz 2 π hbar,
   M → 140. Φ0, d → 0.1, Φ → 0 Φ0, β → 0.00073, CΣ → 4.37 10^-15, T → 0.02};

Plot[T1charge[Flatten[Append[{ng → x}, params]]], {x, 0, 1}, PlotRange → All]
Plot[T1flux[Flatten[Append[{Φ → x Φ0}, params]]], {x, -1, 1}, PlotRange → All]
Clear[Φ0, hbar, kb, GHz];
```

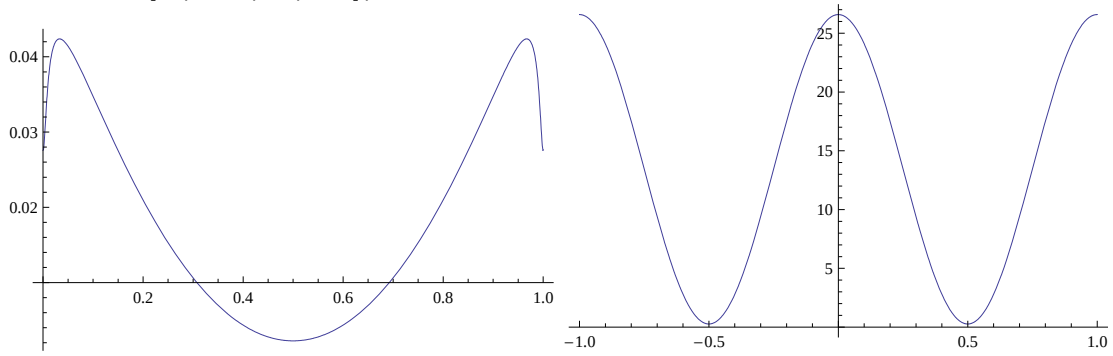

Bibliography

[1] A. Blais, R. S. Huang, A. Wallraff, S. M. Girvin, and R. J. Schoelkopf. Cavity quantum electrodynamics for superconducting electrical circuits: An architecture for quantum computation. *Physical Review A*, 69(6):062320, June 2004.

[2] L. Frunzio, A. Wallraff, D. Schuster, J. Majer, and R. Schoelkopf. Fabrication and characterization of superconducting circuit QED devices for quantum computation. *IEEE Transactions On Applied Superconductivity*, 15(2):860–863, June 2005.

[3] V. Bouchiat, D. Vion, P. Joyez, D. Esteve, and M. H. Devoret. Quantum coherence with a single Cooper pair. *Physica Scripta*, T76:165–170, 1998.

[4] A. Wallraff, D. I. Schuster, A. Blais, L. Frunzio, R. S. Huang, J. Majer, S. Kumar, S. M. Girvin, and R. J. Schoelkopf. Strong coupling of a single photon to a superconducting qubit using circuit quantum electrodynamics. *Nature*, 431:162–167, 2004.

[5] A. Wallraff, D. I. Schuster, A. Blais, L. Frunzio, J. Majer, S. M. Girvin, and R. J. Schoelkopf. Approaching unit visibility for control of a superconducting qubit with dispersive readout. *Physical Review Letters*, 95:060501, 2005.

[6] J. Majer, J. M. Chow, J. M. Gambetta, Jens Koch, B. R. Johnson, J. A. Schreier, L. Frunzio, D. I. Schuster, A. A. Houck, A. Wallraff, A. Blais, M. H. Devoret, S. M. Girvin, and R. J. Schoelkopf. Coupling superconducting qubits via a cavity bus. *Nature*, 449(7161):443–447, September 2007.

[7] Richard Feynman. Simulating physics with computers. *International Journal of Theoretical Physics*, 21(6):467–488, June 1982.

[8] D. Deutsch. Quantum theory, the church-turing principle and the universal quantum computer. *Proceedings of the Royal Society of London. Series A, Mathematical and Physical Sciences*, 400(1818):97–117, July 1985.

[9] David Deutsch and Richard Jozsa. Rapid solution of problems by quantum computation. *Proceedings: Mathematical and Physical Sciences*, 439(1907):553–558, December 1992.

[10] Peter W. Shor. Polynomial-time algorithms for prime factorization and discrete logarithms on a quantum computer. *SIAM Journal on Scientific and Statistical Computing*, 26:1484, 1997.

[11] Lov K. Grover. A fast quantum mechanical algorithm for database search. In *Proceedings of the twenty-eighth annual ACM symposium on Theory of computing*, pages 212–219, Philadelphia, Pennsylvania, United States, 1996. ACM.

[12] Michael A. Nielsen and Isaac L. Chuang. *Quantum Computation and Quantum Information*. Cambridge Univertity Press, 2000.

[13] J. I. Cirac and P. Zoller. Quantum computations with cold trapped ions. *Physical Review Letters*, 74:4091–4094, 1995.

[14] Daniel Loss and David P. DiVincenzo. Quantum computation with quantum dots. *Physical Review A*, 57(1):120–, January 1998.

[15] David G. Cory, Amr F. Fahmy, and Timothy F. Havel. Ensemble quantum computing by NMR spectroscopy. *Proceedings of the National Academy of Sciences*, 94(5):1634–1639, March 1997.

[16] D. M. Pozar. *Microwave Engineering*. Addison-Wesley Publishing Company, 1993.

[17] D. I. Schuster. *Circuit Quantum Electrodynamics*. PhD thesis, Yale University, 2007.

[18] D. Vion, A. Aassime, A. Cottet, P. Joyez, H. Pothier, C. Urbina, D. Esteve, and M. H. Devoret. Rabi oscillations, ramsey fringes and spin echoes in an electrical circuit. *Fortschritte der Physik*, 51:462–468, 2003.

[19] Jens Koch, Terri M. Yu, Jay Gambetta, A. A. Houck, D. I. Schuster, J. Majer, Alexandre Blais, M. H. Devoret, S. M. Girvin, and R. J. Schoelkopf. Charge-insensitive qubit design derived from the Cooper pair box. *Physical Review A*, 76(4):042319, 2007.

[20] Andreas Wallraff, Hannes Majer, Luigi Frunzio, and Robert Schoelkopf. Superconducting solid state cavity QED: Notes on resonators. 2003.

[21] R. N. Simons. *Coplanar waveguide circuits, components and systems*. Wiley Series in Microwave and Optical Engineerging. Wiley Inter-Science, 2001.

[22] D.F. Walls and G.J. Milburn. *Quantum optics*. Spinger-Verlag, Berlin, 1994.

[23] Johannes Fink. Single qubit control and observation of Berry's phase in a superconducting quantum circuit. Master's thesis, Universität Wien, 2007.

[24] R. J. Schoelkopf, A. A. Clerk, S. M. Girvin, K. W. Lehnert, and M. H. Devoret. Qubits as spectrometers of quantum noise. *cond-mat/0210247*, 2002.

[25] J. A. Schreier, A. A. Houck, Jens Koch, D. I. Schuster, B. R. Johnson, J. M. Chow, J. M. Gambetta, J. Majer, L. Frunzio, M. H. Devoret, S. M. Girvin, and R. J. Schoelkopf. Suppressing charge noise decoherence in superconducting charge qubits, 2007.

[26] A. Fukushima, A. Sato, A. Iwasa, Y. Nakamura, T. Komatsuzaki, and Y. Sakamoto. Attenuation of microwave filters for single-electron tunneling experiments. *IEEE Transactions on Instrumentation and Measurement*, 46(2):289–293, 1997.

[27] John M. Martinis, Michel H. Devoret, and John Clarke. Experimental tests for the quantum behavior of a macroscopic degree of freedom: The phase difference across a Josephson junction. *Physical Review B*, 35(10):4682–4698, Apr 1987.

[28] A. Lukashenko and A. V. Ustinov. Improved powder filters for qubit measurements. *Review of Scientific Instruments*, 79(1):014701–4, January 2008.